IMMUNOLOGY

Dual NADPH oxidases DUOX1 and DUOX2 synthesize NAADP and are necessary for Ca^{2+} signaling during T cell activation

Feng Gu[1]†, Aileen Krüger[1]†, Hannes G. Roggenkamp[1]†, Rick Alpers[1], Dmitri Lodygin[2], Vincent Jaquet[3], Franziska Möckl[1], Lola C. Hernandez C.[1], Kai Winterberg[1], Andreas Bauche[1], Anette Rosche[1], Helmut Grasberger[4], John Y. Kao[4], Daniel Schetelig[5], René Werner[5], Katrin Schröder[6], Michael Carty[7], Andrew G. Bowie[7], Samuel Huber[8], Chris Meier[9], Hans-Willi Mittrücker[10], Joerg Heeren[1], Karl-Heinz Krause[3], Alexander Flügel[2], Björn-Philipp Diercks[1]‡, Andreas H. Guse[1]*‡

The formation of Ca^{2+} microdomains during T cell activation is initiated by the production of nicotinic acid adenine dinucleotide phosphate (NAADP) from its reduced form NAADPH. The reverse reaction—NAADP to NAADPH—is catalyzed by glucose 6-phosphate dehydrogenase (G6PD). Here, we identified NADPH oxidases NOX and DUOX as NAADP-forming enzymes that convert NAADPH to NAADP under physiological conditions in vitro. T cells express NOX1, NOX2, and, to a minor extent, DUOX1 and DUOX2. Local and global Ca^{2+} signaling were decreased in mouse T cells with double knockout of *Duoxa1* and *Duoxa2* but not with knockout of *Nox1* or *Nox2*. Ca^{2+} microdomains in the first 15 s upon T cell activation were significantly decreased in *Duox2*$^{-/-}$ but not in *Duox1*$^{-/-}$ T cells, whereas both DUOX1 and DUOX2 were required for global Ca^{2+} signaling between 4 and 12 min after stimulation. Our findings suggest that a DUOX2- and G6PD-catalyzed redox cycle rapidly produces and degrades NAADP through NAADPH as an inactive intermediate.

INTRODUCTION

Ca^{2+} microdomains are the earliest signaling events observed upon T cell activation (*1*). These localized, short-lived, and highly dynamic signaling events originate from both Ca^{2+} entry and Ca^{2+} release (*1*, *2*). Ca^{2+} microdomains merge into global Ca^{2+} signals in T cells about 20 to 30 s after stimulation. Preformed clusters of stromal interaction molecule (STIM) proteins and ORAI1 allow for less frequent and smaller Ca^{2+} microdomains in the absence of stimulation of the T cell receptor (TCR)/CD3 complex, thereby providing a basic excitability to enable fast and efficient activation of Ca^{2+} signaling if the TCR/CD3 complex is triggered (*2*). This transition from small and infrequent Ca^2 microdomains toward the highly dynamic Ca^{2+} microdomains evoked by TCR/CD3 stimulation proceeds by formation of the Ca^{2+}-mobilizing second messenger nicotinic acid adenine dinucleotide phosphate (NAADP) within seconds after TCR/CD3 stimulation (*3*). In T cells, NAADP binds to a recently discovered NAADP binding protein, termed hematological and neurological expressed 1–like protein (HN1L)/Jupiter microtubule associated homolog 2 (JPT2) (*4*, *5*). Either HN1L/JPT2 is in complex with ryanodine receptor type 1 (RYR1) and then binds NAADP, or cytosolic HN1L/JPT2 binds NAADP and then the complex binds to RYR1. The assembly of HN1L/JPT2 and NAADP binds to RYR1 and then activates Ca^{2+} release through RYR1 localized at the endoplasmic reticulum (ER) (*6*–*8*). This prominent role of the NAADP-HN1L/JPT2-RYR1 axis in Ca^{2+} microdomain formation was demonstrated by knockout of HN1L/JPT2 or RYR1 (*1*, *2*, *4*). Moreover, downstream T cell activation events are affected by NAADP antagonism, resulting in decreased translocation of nuclear factor of activated T cells (NFAT), diminished expression of proinflammatory cytokines, and attenuated clinical scores in rat experimental autoimmune encephalomyelitis (*9*, *10*).

One question remained, however: How is NAADP produced in cells? Given the importance of NAADP signaling for Ca^{2+} microdomains and T cell activation, the central goal of this study was to identify the NAADP-forming enzyme in T cells using Ca^{2+} microdomain formation as a readout for NAADP synthesis.

RESULTS

Knockout of CD38 affects neither initial Ca^{2+} microdomains nor global Ca^{2+} signals in primary T cells

Previously, it was shown in a cell-free system that NAD-glycohydrolase/ADP-ribosyl cyclase CD38 can produce NAADP from NADP, but also degrades NAADP to 2′-phospho-adenosine diphosphoribose (ADPR) (*11*, *12*). However, in intact primary *Cd38*$^{-/-}$ T cells, the number of Ca^2 microdomains was not different from wild-type (WT) controls within 15 s after simultaneous stimulation of TCR/CD3 and CD28 (Fig. 1, A to C). Further, global Ca^{2+} signaling was not affected in *Cd38*$^{-/-}$ T cells, except for a slightly decreased basal Ca^{2+} concentration,

[1]Calcium Signaling Group, Department of Biochemistry and Molecular Cell Biology, University Medical Center Hamburg-Eppendorf, 20246 Hamburg, Germany. [2]Institute for Neuroimmunology and Multiple Sclerosis Research, University Medical Center Göttingen, 37075 Göttingen, Germany. [3]Department of Pathology and Immunology, University of Geneva, 1211 Geneva 4, Switzerland. [4]Department of Internal Medicine, Division of Gastroenterology, University of Michigan, Ann Arbor, MI 48109, USA. [5]Department of Computational Neuroscience, University Medical Center Hamburg-Eppendorf, Hamburg 20246, Germany. [6]Institute of Cardiovascular Physiology, Goethe-Universität, 60590 Frankfurt, Germany. [7]School of Biochemistry and Immunology, Trinity Biomedical Sciences Institute, Trinity College Dublin, Dublin 2, Ireland. [8]Department of Gastroenterology with Sections Infectiology and Tropical Medicine, University Medical Center Hamburg-Eppendorf, 20246 Hamburg, Germany. [9]Organic Chemistry, University of Hamburg, 20146 Hamburg, Germany. [10]Department of Immunology, University Medical Center Hamburg-Eppendorf, 20246 Hamburg, Germany.
*Corresponding author. Email: guse@uke.de
†These authors contributed equally to this work.
‡These authors contributed equally to this work.

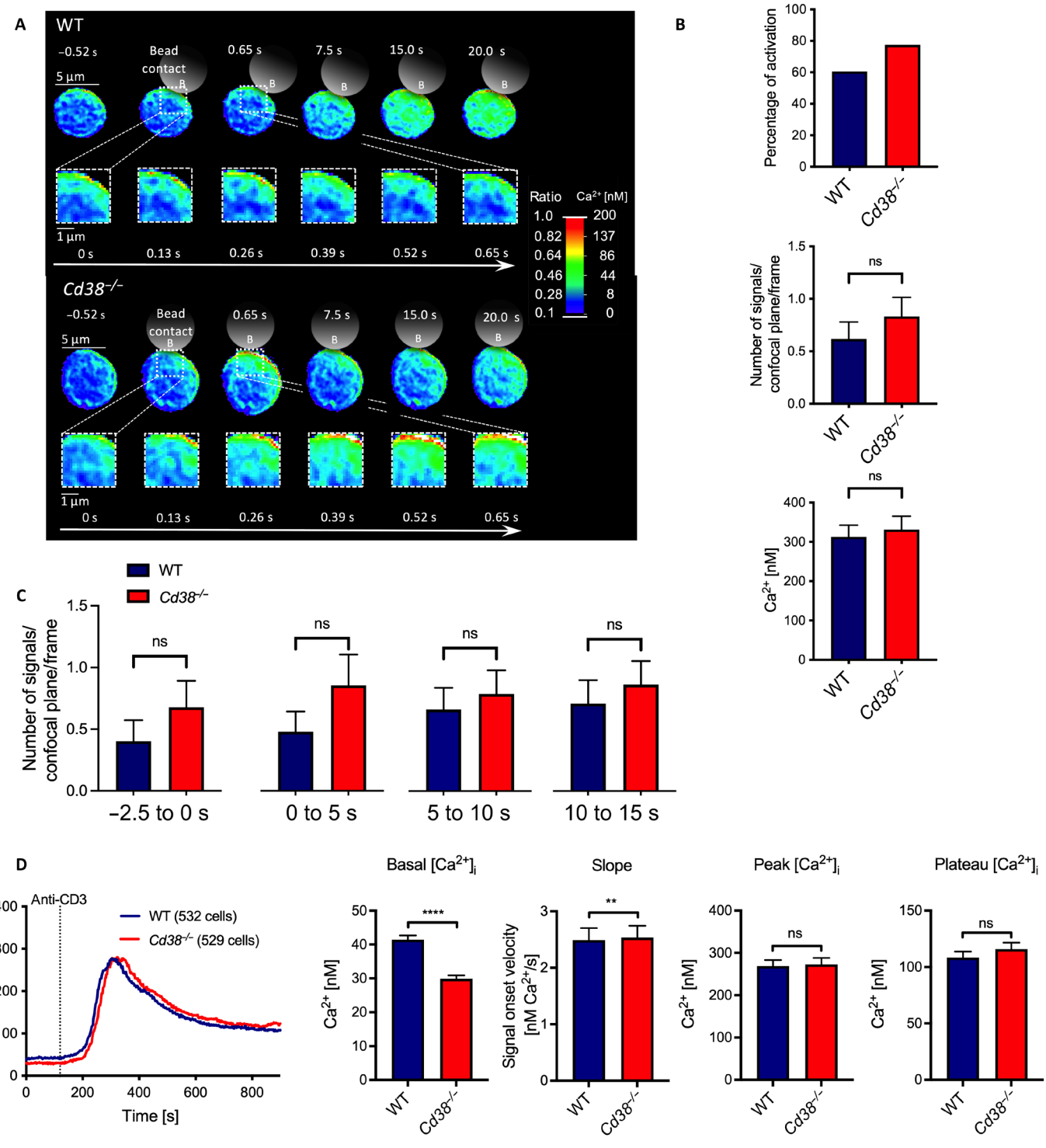

Fig. 1. Knockout of CD38 does not affect initial Ca^{2+} microdomains or global Ca^{2+} signals in primary T cells. (**A**) Representative high-resolution Ca^{2+} images of WT (top) and *Cd38*$^{-/-}$ (bottom) $CD4^+$ T cells loaded with both Fluo4-AM and Fura-Red-AM after stimulation with anti-CD3/anti-CD28–coated bead (schematically indicated). The heatmap indicates emission ratios between Fluo-4 and Fura-Red ranging from 0.1 to 1.0; ratio data were then converted using external calibration corresponding to 0 to 200 nM $[Ca^{2+}]_i$. Scale bars, 5 µm (whole cells) and 1 µm (magnified region). (**B**) Analysis across the first 15 s of stimulation shown as percentage of activated cells, number of Ca^{2+}microdomains, and average Ca^{2+} concentration of the microdomains. Data are means ± SEM; WT, $n = 38$ cells; *Cd38*$^{-/-}$, $n = 31$ cells. ns, not significant using a nonparametric Mann-Whitney *U* test. (**C**) Analysis of the number of Ca^{2+} microdomains per confocal sublayer and frame from (B) at different time points (as indicated) before and after bead stimulation. Statistical analysis as in (B). (**D**) Analysis of global Ca^{2+} measurements in $CD4^+$ T cells from WT or *Cd38*$^{-/-}$ mice, showing mean Ca^{2+} traces upon anti-CD3 addition, basal Ca^{2+} concentration, signal onset after 150 s, and peak and plateau amplitudes. Data are means ± SEM; WT, $n = 532$ cells; *Cd38*$^{-/-}$, $n = 529$ cells. Nonparametric Mann-Whitney *U* test: $^{**}P < 0.005$, $^{****}P < 0.0001$.

as reported previously (Fig. 1D) (*13*). These data suggest that CD38 is not the enzyme forming NAADP acutely upon TCR/CD3 stimulation, consistent with previous results showing that NAADP formation by CD38 via the base-exchange reaction proceeds at nonphysiological conditions (pH 4 to 5, millimolar concentrations of nicotinic acid necessary) (*11*). Along this line, endogenous levels of NAADP were either unaffected or increased in tissues from *Cd38*$^{-/-}$ mice (*12*, *14*).

NADPH oxidases (NOX/DUOX) synthesize NAADP from its reduced form NAADPH

It has long been known that NADPH oxidases (NOX/DUOX enzymes, EC 1.6.3.1) oxidize NADPH to NADP while producing reactive oxygen species (ROS). Therefore, we hypothesized that also NAADPH, which itself is not a Ca^{2+}-mobilizing compound (*15*), may be used as substrate by NOX/DUOX to produce NAADP. NAADPH was prepared by chemical reduction as described (*15*), and purity of the product was confirmed by high-performance liquid chromatography (HPLC) (fig. S1, A and B). Using membranes from human embryonic kidney (HEK) cells recombinantly expressing NOX5, DUOX1, or DUOX2, synthesis of NAADP from NAADPH was observed under physiological conditions in a cell-free system (Fig. 2, A and B). NOX5 can be easily expressed as an active enzyme in HEK cells and was used as model enzyme. The identity of NAADP produced by NOX5 was confirmed by HPLC retention time and loss of photometric signal at 340 nm (Fig. 2A and fig. S1C). Michaelis-Menten kinetics for NOX5 resulted in quite similar maximum velocities and K_m values for substrates NADPH and NAADPH (Fig. 2A). However, for NOX5, the pH optimum for NAADPH was about 7.5, whereas it was >8 for NADPH (Fig. 2A). In addition, both recombinant DUOX1 and DUOX2 convert NAADPH to NAADP, as confirmed by HPLC retention time and loss of photometric signal at 340 nm (Fig. 2B). Whereas DUOX1 preferred NADPH over NAADPH as substrate, there was no significant difference for either NADPH or NAADPH as substrate for DUOX2 (Fig. 2B). T cell membranes catalyzed formation of NAADP from NAADPH (Fig. 2C), and NAADP was further metabolized to adenosine 5′-monophosphate (AMP) (Fig. 2C). These results open the principal possibility of NAADP being formed by oxidation and transferred back into the reduced form by a redox cycle. Accordingly, we tested the major enzymes known to reduce NADP, namely, glucose 6-phosphate dehydrogenase (GLC-6-P-DH), 6-phosphogluconate dehydrogenase, isocitrate dehydrogenase, or malate dehydrogenase for substrate NAADP. The backward reaction from NAADP to NAADPH is catalyzed by GLC-6-P-DH (Fig. 2D and fig. S1D), but not by any of the other major cellular dehydrogenases tested (fig. S2, A to D). Identity of product NAADPH was confirmed by HPLC retention time and the increase in photometric signal at 340 nm (Fig. 2D). The K_m value for NAADP was 2.30 ± 1.13 μM, thus displaying a much higher affinity for GLC-6-P-DH as compared with 44.47 ± 17.74 μM for NADP (Fig. 2D). The maximum velocity, however, was significantly smaller for NAADP versus NADP (Fig. 2D). These data suggest that GLC-6-P-DH according to its very high affinity for NAADP may convert low cytosolic [NAADP] back to NAADPH, hereby explaining the rapid decline of endogenous [NAADP] between 10 and 20 s after TCR/CD3 stimulation (*3*). Thus, we suggest a redox cycle where the second messenger NAADP is synthesized by NOX/DUOX, whereas inactive NAADPH is produced by GLC-6-P-DH (fig. S3). Providing the necessary pool of NAADPH for the proposed redox cycle may proceed by slow but continuous formation of NAADP by CD38 or sterile alpha and Toll-interleukin-1 receptor (TIR) motif containing1 [SARM1; (*16*–*18*)], reaching basal NAADP level and then further via GLC-6-P-DH by reduction to NAADPH (fig. S3). Such fill-up reactions may happen even in the absence of cell stimulation as a "housekeeping" function.

Functional knockout of DUOX1/DUOX2 affects global Ca^{2+} signaling in T cells

Of the various isoforms of the NOX/DUOX family, NOX1, NOX2, and, to a minor extent, also DUOX1 and DUOX2 are expressed in mouse and rat T cells (fig. S4, A and B). Both DUOX1 and DUOX2 are localized in discrete spots in the plasma membrane and also below the plasma membrane, as demonstrated by stimulated emission depletion (STED) super-resolution microscopy (fig. S4C). The specificity of antibodies to DUOX was validated using *Duox1*$^{-/-}$ and *Duox2*$^{-/-}$ T cells (fig. S4D).

Given that antagonism of NAADP or deletion of NAADP receptor HN1L/JPT2 both resulted in characteristic alterations of TCR/CD3-evoked global Ca^{2+} signaling, such as delayed signal onset and decreased but not fully abrogated peak and plateau Ca^{2+} signals (*4*, *9*), we used global Ca^{2+} signaling over about 800 s after stimulation in respective gene silencing models to test for a role of the different NOX/DUOX isozymes. Neither T cells from *Nox1*$^{-/-}$ nor T cells from *Nox2*$^{-/-}$ mice were different in free cytosolic Ca^{2+} concentration ($[Ca^{2+}]_i$) at signal onset, peak, or plateau (Fig. 3, A to D); global Ca^{2+} signaling data for *Cd38*$^{-/-}$ were also not different from WT controls (Fig. 1D). In contrast to *Nox2*$^{-/-}$, *Nox1*$^{-/-}$, or *Cd38*$^{-/-}$ T cells, global Ca^{2+} signaling was significantly decreased in *Duoxa1*$^{-/-}$/*Duoxa2*$^{-/-}$ T cells (Fig. 3, B to D). The maturation factors DUOXA1 and DUOXA2 are necessary for trafficking of DUOX1 and DUOX2 from rough ER toward the plasma membrane (*19*). Thus, DUOX1 or DUOX2 enzymatic activity is absent in the plasma membrane of *Duoxa1*$^{-/-}$/*Duoxa2*$^{-/-}$ T cells (*19*, *20*).

Functional knockout of DUOX1/DUOX2 blocks Ca^{2+}microdomain formation in the first seconds of T cell activation

Ca^{2+} microdomains evoked by TCR/CD3 stimulation were also decreased in *Duoxa1*$^{-/-}$/*Duoxa2*$^{-/-}$ T cells. Within the first 25 s after TCR/CD3 stimulation, the number of Ca^{2+} microdomains was significantly decreased in *Duoxa1*$^{-/-}$/*Duoxa2*$^{-/-}$ T cells (Fig. 4, A and B). This effect was observed already in the first second after stimulation (Fig. 4C). This time period fits very well with NAADP kinetics upon TCR/CD3 stimulation where the endogenous [NAADP] rose rapidly within 10 s after TCR/CD3 stimulation and declined back to almost basal levels within the next 10 s (*3*).

Knockout of DUOX2, but not DUOX1, affects Ca^{2+}microdomain formation in the first seconds of T cell activation

Ca^{2+} microdomains evoked by TCR/CD3 stimulation were then recorded in rat T cells with single gene knockouts of *Duox1* or *Duox2* designed by CRISPR-CAS technology (Fig. 5, A to C, and fig. S5, A and B). Both DUOX1 and DUOX2 were localized to the plasma membrane in STED super-resolution microscopy (fig. S4C). Whereas WT rat T cells responded with similar rapid and dynamic kinetics of Ca^{2+} microdomains, there was not much difference for T cells with deletion of *Duox1*$^{-/-}$ (Fig. 5A). However, for *Duox2*$^{-/-}$ T cells,

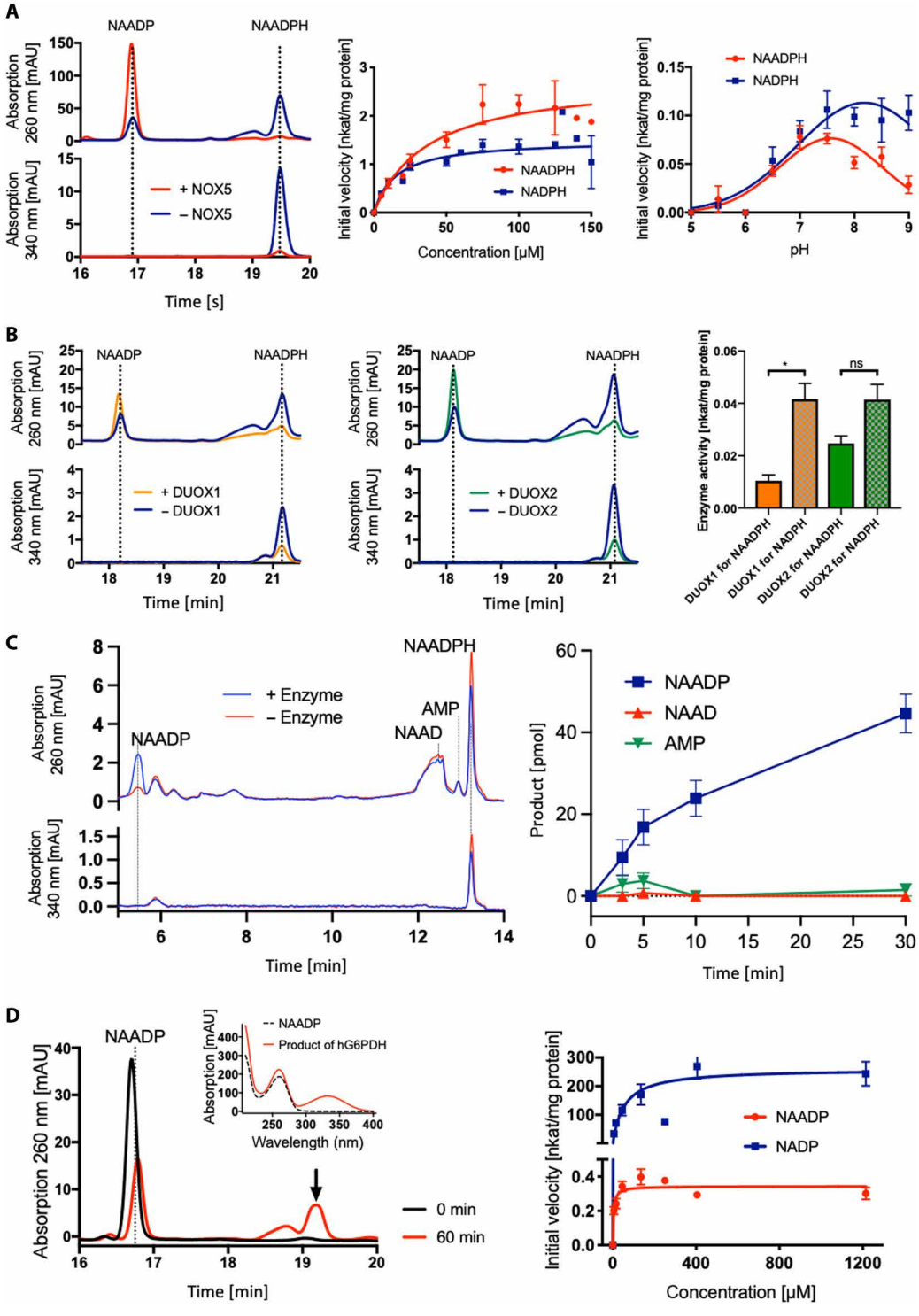

Fig. 2. NOX/DUOX enzymes synthesize NAADP from its reduced form NAADPH. (**A**) Synthesis of NAADP from NAADPH (produced by chemical reduction; purified and quantified by semipreparative HPLC; fig. S1) in the presence or absence of NOX5-containing HEK cell membranes (0.01 mg protein/ml) using 5 to 200 μM NADPH or NAADPH, 5.5 μM phosphatidic acid, 700 μM $CaCl_2$, 1 mM $MgCl_2$, 450 μM NTA, 450 μM EDTA, 10 μM FAD, and 50 mM Hepes at pH 7.4. Substrates and products were separated by reversed phase (RP)–HPLC as described in Materials and Methods. A representative of three experiments is shown. Right: Reaction velocity of NOX5 for Michaelis-Menten kinetics, and pH dependency was analyzed through decrease of optical absorbance of NAADPH at 340 nm. Data are means ± SEM, $n = 3$ independent experiments. (**B**) Synthesis of NAADP from NAADPH in the presence or absence of DUOX1- or DUOX2-containing HEK cell membranes (0.25 mg protein/ml) using 50 μM NAADPH, 5.5 μM phosphatidic acid, 1.4 mM $CaCl_2$, 1 mM $MgCl_2$, 450 μM NTA, 450 μM EDTA, 10 μM FAD, and 50 mM Hepes at pH 7.1. HPLC conditions were as described in (A). A characteristic HPLC chromatogram of five experiments is shown. Right: Bar chart compares enzyme activity toward NAADPH and NADPH. Data are means ± SEM, $n = 5$ independent experiments. Nonparametric Mann-Whitney *U* test: $^*P < 0.05$. (**C**) Formation of NAADP from NAADPH by membranes from WT Jurkat T cells (0.75 mg protein/ml) using 50 μM NAADPH, 5.5 μM phosphatidic acid, 1.4 mM $CaCl_2$, 1 mM $MgCl_2$, 450 μM NTA, 450 μM EDTA, 10 μM FAD, and 50 mM Hepes at pH 7.1. For negative controls, FAD was omitted and NOX/DUOX inhibitor DPI (5 μM) was added to the incubation buffer. HPLC conditions as described in (A). A representative of four experiments is shown. Right: Kinetics of NAADP, NAAD, and AMP. Data are means ± SEM, $n = 3$ independent experiments. (**D**) Left: Production of NAADPH from NAADP by recombinant GLC-6-P-DH (0.2 U/ml) using 10 μM NAADP, 50 mM glucose 6-phosphate, and 20 mM Hepes at pH 7.4. Inset shows absorbance of NAADP and the product formed by GLC-6-P-DH. HPLC conditions as in (A). A representative of three experiments is shown. Right: Reaction velocity of GLC-6-P-DH for Michaelis-Menten kinetics, and pH dependency was analyzed through decrease of optical absorbance of NAADPH or NADPH at 340 nm. Data are means ± SEM, $n = 3$ independent experiments. mAU, milli absorbance units.

a significantly decreased number of Ca^{2+} microdomains was observed (Fig. 5, A and B), particularly in the first second (Fig. 5C). Within the first 22 s, Ca^{2+} microdomains linearly recovered (Fig. 5B). However, a clear difference between WT and *Duox2*$^{-/-}$ was observed, suggesting that DUOX2 is the enzyme synthesizing NAADP within seconds after stimulation, a process that cannot be replaced by DUOX1 in the very beginning of signaling. However, gradually, DUOX1 takes over the role of DUOX2 (in *Duox2*$^{-/-}$), and from about 22 s on, there is almost

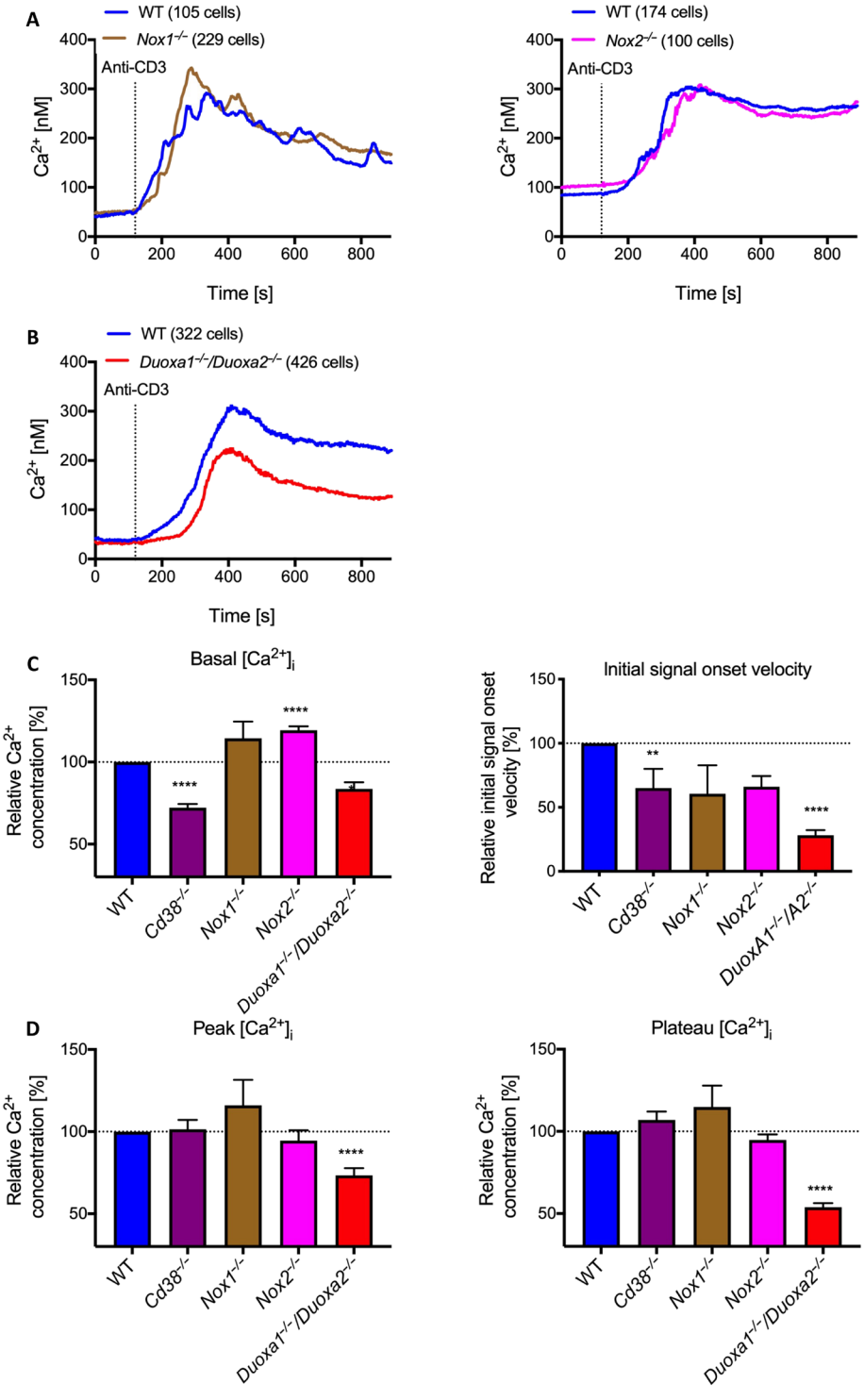

Fig. 3. Effect of knockout of *Cd38*, *Nox1*, *Nox2*, and *Duoxa1*/*Duoxa2* on global Ca^{2+} signaling in primary T cells. (**A** to **D**) Analysis of global Ca^{2+} measurements in $CD4^+$ T cells freshly isolated and loaded with Fura2-AM from (A) WT, *Nox1*$^{-/-}$, *or Nox2*$^{-/-}$ mice or (B) WT or *Duoxa1*$^{-/-}$/*Duoxa2*$^{-/-}$ mice showing mean Ca^{2+} traces upon addition of CD3 antibody (10 μg/ml). *N* = number of cells as indicated. Aggregated data are (C) basal Ca^{2+} concentration and signal onset velocity or (D) Ca^{2+} peak and plateau amplitudes; as means ± SEM, *n* given in (A) and (B); *n* = 529 *Cd38*$^{-/-}$ T cells and *n* = 532 WT controls. Nonparametric Mann-Whitney *U* test: $^{**}P < 0.005$, $^{****}P < 0.0001$.

no difference regarding the number of Ca^{2+} microdomains (Fig. 5C).

Knockout of Duox2 or Duox1 differentially affects global Ca^{2+} signaling in T cells

Next, we explored how knockout of *Duox1* or *Duox2* would affect global Ca^{2+} signaling. In *Duoxa1*$^{-/-}$/*Duoxa2*$^{-/-}$ T cells, the functional double knockout of DUOX1 and DUOX2, global Ca^{2+} signaling was characterized by a delayed signal onset and decreased Ca^{2+} peak and plateau amplitudes (described above, Fig. 3, B to D). Within the first 2 min upon TCR/CD3 stimulation, for both *Duox2*$^{-/-}$ and *Duox1*$^{-/-}$ T cells, a delayed signal onset velocity and decreased Ca^{2+} plateau amplitude were observed; *Duox2*$^{-/-}$ T cells additionally showed a diminished Ca^{2+} peak amplitude (Fig. 6A).

Moreover, also in the Ca^{2+} plateau phase, significantly decreased signaling was observed for both *Duox1*$^{-/-}$ or *Duox2*$^{-/-}$ T cells (Fig. 6A). Next, the *Duox* knockout phenotypes were further subjected to NAADP antagonism using NAADP antagonist BZ194 (Fig. 6, B to D). In WT T cells, BZ194 decreased all parameters (signal onset velocity, Ca^{2+} peak, and plateau amplitudes; Fig. 6B), as reported earlier (*4*, *9*). When applying BZ194 to *Duox1*$^{-/-}$ T cells, signal onset velocity was markedly reduced, whereas Ca^{2+} peak or plateau amplitudes were not altered as compared with the vehicle control (Fig. 6C), indicating that in the early phase of TCR/CD3 stimulation, BZ194 inhibits a signaling component other than *Duox1*$^{-/-}$. The same experiment carried out with *Duox2*$^{-/-}$ T cells resulted in almost identical signal onset velocity, Ca^{2+} peak, and plateau amplitudes in the presence or absence of BZ194 (Fig. 6D). Collectively, these data confirm DUOX2 as the enzyme that synthesizes NAADP in the first seconds and minutes of T cell activation. In addition, the decreased Ca^{2+} plateau phase in *Duox1*$^{-/-}$ T cells indicates a role for this isozyme in the period later than about 3 min after TCR/CD3 stimulation.

H_2O_2 produced by DUOX2 in the first seconds of T cell activation does not stimulate Ca^{2+} microdomain formation

In addition to NAADP, DUOX isozymes produce H_2O_2 that potentially may affect Ca^{2+} signaling. Because cytosolic NAADP concentrations upon TCR/CD3 stimulation did not exceed 40 nM (*3*), [H_2O_2] is expected to be in a similar low nanomolar range. Further, the H_2O_2-producing peroxidase-homology domain of DUOX is located at the

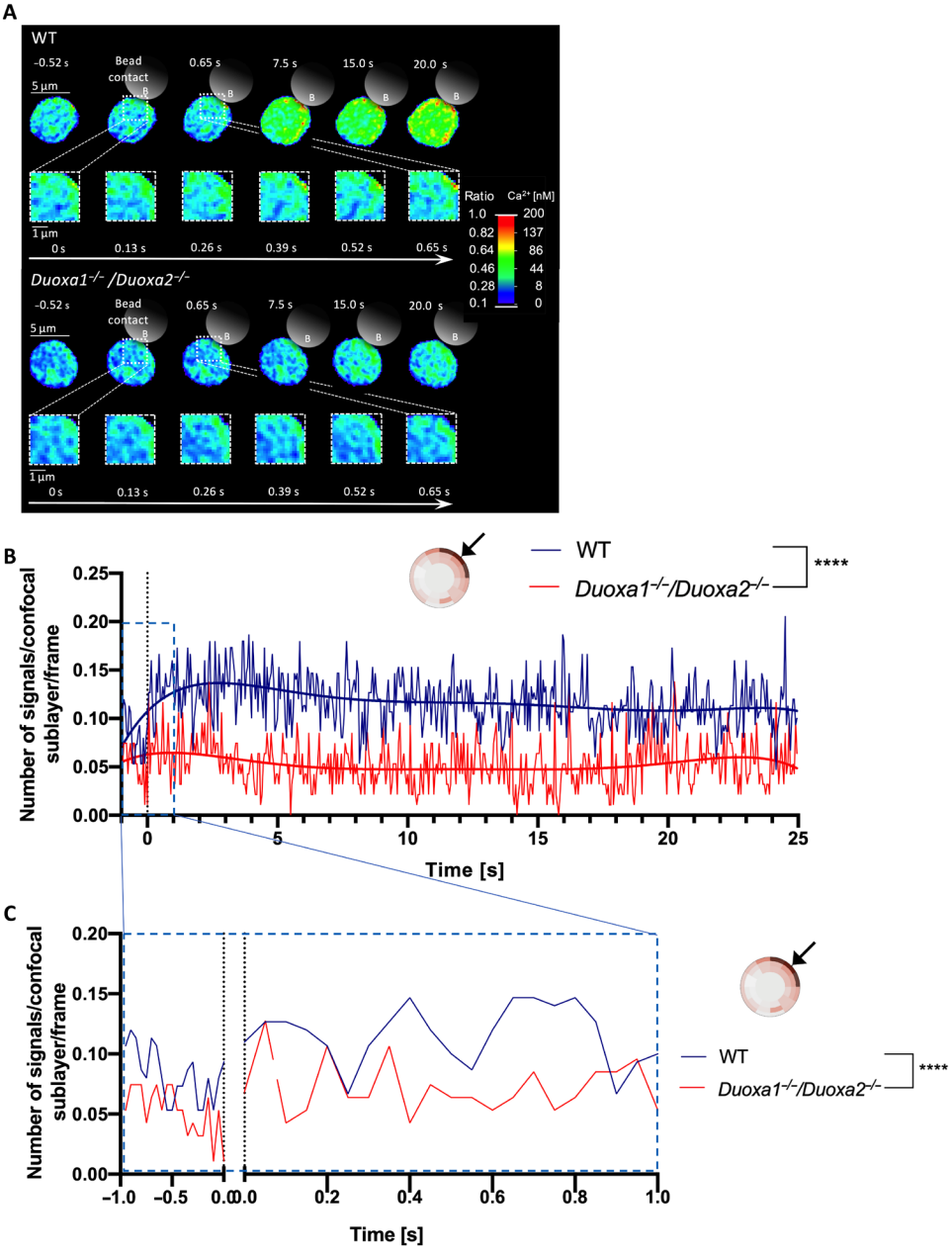

Fig. 4. Knockout of both *Duoxa1* and *Duox*a2 significantly decreased the formation of initial Ca^{2+} microdomains in primary T cells. (**A**) Representative high-resolution Ca^{2+} images of WT (top) and *Duoxa1*$^{-/-}$/*Duoxa2*$^{-/-}$ (bottom) T cells loaded with both Fluo4-AM and Fura-Red-AM after stimulation with an anti-CD3/anti-CD28–coated bead (schematically indicated). The heatmap indicates emission ratios between Fluo-4 and Fura-Red ranging from 0.1 to 1.0; ratio data were then converted using external calibration corresponding to 0 to 200 nM $[Ca^{2+}]_i$. Scale bars, 5 µm for whole cells, 1 µm for magnified region. (**B**) Kinetics of the number of Ca^{2+}microdomains in the subcellular layers below the plasma membrane, as indicated in the inset, close to the stimulating bead (indicated by arrow) 1 s before and in the first 25 s after stimulation. Data are means ± SEM (blue: WT, $n = 75$ cells; red: *Duoxa1*$^{-/-}$/*Duoxa2*$^{-/-}$, $n = 52$ cells) from seven independent experiments. To better visualize kinetics of activation, data were fitted using a nonlinear sixth-order polynomial function. ****$P < 0.0001$ by a nonparametric Mann-Whitney *U* test. (**C**) Magnification of the first second after T cell stimulation (= contact of anti-CD3/anti-CD28–coated bead). Statistical analysis as in (B).

outer leaflet of the plasma membrane, resulting in H_2O_2 release into the extracellular space (Fig. 7A). Likely, H_2O_2 will rapidly diffuse away from the cell, thereby lowering the concentration at the plasma membrane. To study effects of this portion of H_2O_2, TCR/CD3-evoked Ca^{2+} microdomains were analyzed in the presence of H_2O_2-degrading catalase in the extracellular space. However, neither the percentage of activated cells or the number or the amplitude of Ca^{2+} microdomains (Fig. 7B), nor global Ca^{2+} signaling (fig. S6, A to C) was significantly altered. Next, we considered uptake of H_2O_2 into T cells via aquaporins, such as H_2O_2-transporting aquaporins 3 or 8 (*21*). Because aquaporin 8 is not expressed in T cells (*22*), aquaporin 3 inhibitor DFP00173 was used (*23*). Again, no differences in the three parameters "percentage of activated cells" and "number or amplitude of Ca^{2+} microdomains" were observed (Fig. 7C and fig. S7, A and B). These results were confirmed by analysis of Ca^{2+} microdomains in cells loaded with the ROS scavenger butylated hydroxyanisole (BHA) (Fig. 7D and fig. S7). In addition, we analyzed the concentration of H_2O_2 in the cytosol just below the plasma membrane using the H_2O_2 sensor HyPer7 in its plasma membrane bound form (*24*). Addition of extracellular concentrations of H_2O_2 exceeding the expected concentration reached by DUOX activity, such as 10 µM or 400 nM, resulted in H_2O_2 uptake into the T cell, whereas 80 to 200 nM exogenous H_2O_2 did not cause measurable uptake (Fig. 7, E and F). TCR/CD3 stimulation did not increase the HyPer7 signal above background (buffer addition; Fig. 7, E and F). Last, we added 80 nM H_2O_2 to the extracellular medium while analyzing Ca^{2+} microdomains (Fig. 7G), and despite only about 40 nM H_2O_2 is expected, we did not observe a significant increase in Ca^{2+} microdomain numbers within the first 15 s of TCR/CD3 stimulation, whereas thapsigargin (TG) evoked increased numbers of Ca^{2+} microdomain from 10 s on (Fig. 7H). In summary, our results from these experiments suggest no major role of the second DUOX product H_2O_2 on Ca^{2+} microdomains in the first seconds of TCR/CD3 stimulation.

Knockout of DUOX2 or DUOX1 differentially affects T cell cytokine expression

Next, we asked whether knockout of *Duox* genes in T cells would affect expression of cytokines. Two experimental approaches were used: stimulation by soluble antibody to CD3 (anti-CD3) (Fig. 8A) and stimulation by antigen-pulsed thymic antigen-presenting cells (Fig. 8B). Statistically significant

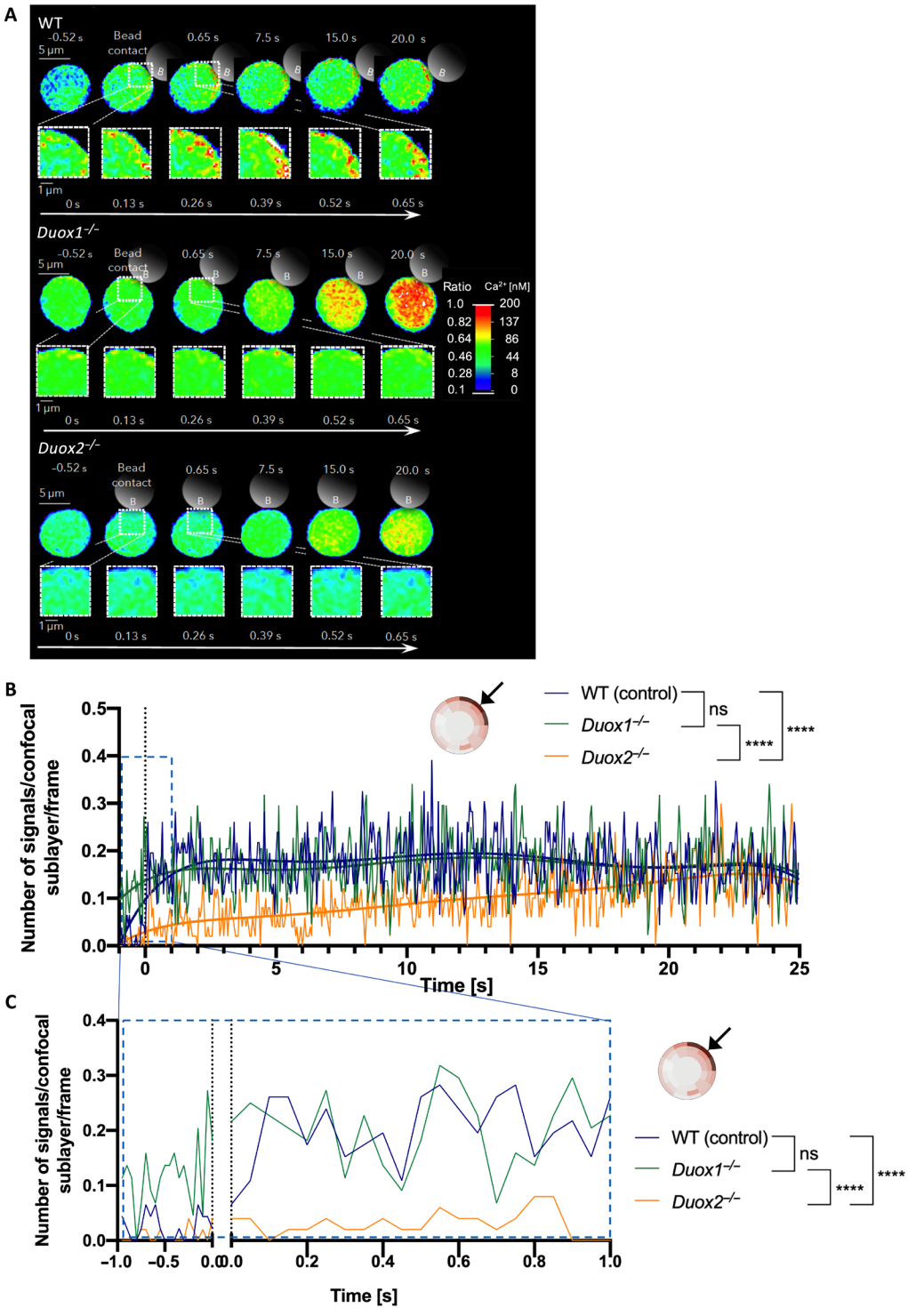

Fig. 5. Single knockouts of *Duox1* or *Duox2* differentially affect the formation of initial Ca^{2+} microdomains in $CD4^+$ effector T cells. (**A**) Representative high-resolution Ca^{2+} images of WT (top) and *Duox1*$^{-/-}$ (middle) and *Duox2*$^{-/-}$ (bottom) rat $CD4^+$ effector T cells loaded with both Fluo4-AM and Fura-Red after stimulation with an anti-CD3/anti-CD28–coated bead (schematically indicated). The heatmap indicates emission ratios between Fluo-4 and Fura-Red ranging from 0.1 to 1.0; ratio data were then converted using external calibration corresponding to 0 to 200 nM $[Ca^{2+}]_i$. Scale bars, 5 μm (whole cells), 1 μm (magnified region). (**B**) Kinetics of the number of Ca^{2+}microdomains in the subcellular layers below the plasma membrane (as indicated in the inset) close to the stimulating bead (as indicated by arrow) 1 s before and in the first 25 s upon T cell activation. Data are means from three independent experiments; blue, WT, $n = 23$ cells; green, *Duox1*$^{-/-}$ $n = 23$ cells; yellow, *Duox2*$^{-/-}$, $n = 25$ cells. To better visualize kinetics of activation, data were fitted using a nonlinear sixth-order polynomal function. ****$P < 0.0001$ by nonparametric Kruskal-Wallis test and Dunn's correction for multiple testing. (**C**) Magnification of the first second after T cell stimulation (= contact of anti-CD3/anti-CD28–coated bead). Statistical analysis as in (B).

effects were seen for *Duox2*$^{-/-}$ or *Duox1*$^{-/-}$ on *Il2* expression, as early cytokine necessary for T cell proliferation and survival (Fig. 8, A and B). Expression of *Il17*, a marker for differentiation into proinflammatory T helper type 17 (T_H17) cells, was suppressed upon anti-CD3 stimulation (Fig. 8A) for both *Duox2*$^{-/-}$ and *Duox1*$^{-/-}$, and for antigenic stimulation only for *Duox2*$^{-/-}$ (Fig. 8B). Expression of *Ifng*, the hallmark cytokine of proinflammatory T_H1 cells, was decreased for both *Duox2*$^{-/-}$ and *Duox1*$^{-/-}$ in both stimulation conditions (Fig. 8, A and B). Together, these cytokine expression data confirm the role of DUOX isozymes in regulating the effector function of T cells.

DISCUSSION

Although NAADP was first described in 1995 (*25*), the biochemical pathway of its formation upon cell stimulation has not yet been resolved. CD38 and SARM1 can produce NAADP in a cell-free system at low pH in the presence of high concentrations of nicotinic acid (*11*, *18*), suggesting NAADP formation in lysosomes (*26*). However, neither Ca^{2+} microdomains nor global Ca^{2+} signaling was affected in acutely stimulated *Cd38*$^{-/-}$ T cells. Nevertheless, SARM1 and/or CD38 may be involved in the fill-up reaction(s) of the redox cycle by slowly producing basal concentrations of NAADP [4.4 ± 1.6 nM;

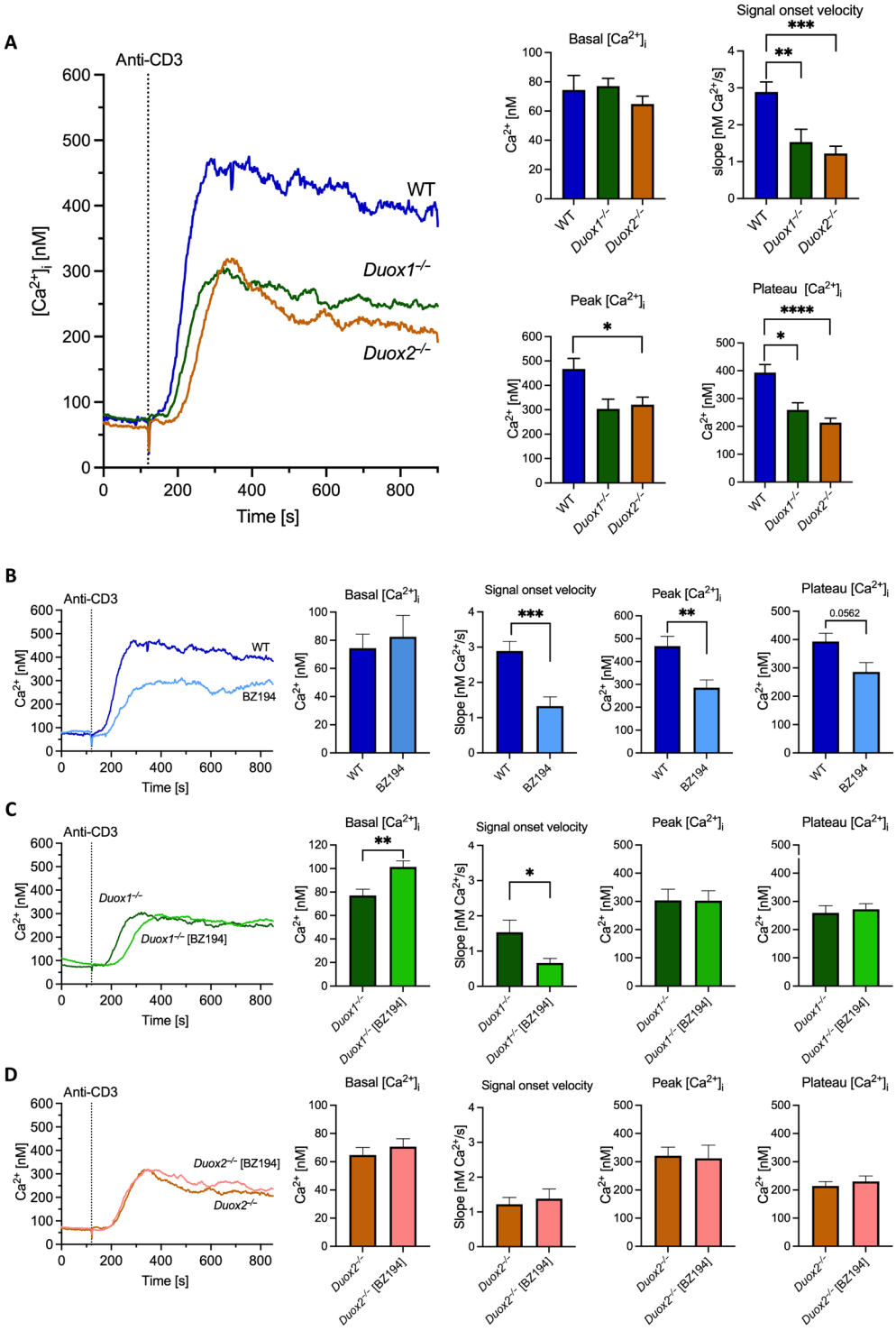

Fig. 6. Single knockouts of *Duox1* or *Duox2* differentially affect global Ca^{2+} signaling in CD4$^+$ effector T cells. (**A**) Comparison of global Ca^{2+} signaling in WT versus *Duox1*$^{-/-}$ or *Duox2*$^{-/-}$ T cells loaded with Fura-2. Left: Kinetics of mean Ca^{2+} traces upon anti-CD3 stimulation (1 μg/ml). Right: Basal Ca^{2+} concentration, signal onset velocity, peak Ca^{2+} concentration, and plateau Ca^{2+} concentration. Data are means ± SEM from $n = 79$ (WT), 38 (*Duox1*$^{-/-}$) cells, and 84 (*Duox2*$^{-/-}$) cells. *$P < 0.05$, **$P < 0.005$, ***$P < 0.001$, ****$P < 0.0001$ by nonparametric Kruskal-Wallis test and Dunn's correction for multiple testing. (**B**) Comparison of DMSO-treated WT versus NAADP antagonist BZ194-treated WT T cells. Both DMSO and BZ194 (500 μM in DMSO) treatments of cells overnight at 1% DMSO (v/v). Left: Kinetics of mean Ca^{2+} traces upon anti-CD3 stimulation (1 μg/ml). Right: Basal Ca^{2+} concentration, signal onset velocity, peak Ca^{2+} concentration, and plateau Ca^{2+} concentration. Data are means ± SEM from $n = 79$ (WT) or 47 (WT/BZ194) cells. **$P < 0.005$, ***$P < 0.001$ by a nonparametric Mann-Whitney *U* test. (**C**) Comparison of DMSO-treated *Duox1*$^{-/-}$ versus BZ194-treated *Duox1*$^{-/-}$ T cells, treated as in (B). Left: Kinetics of mean Ca^{2+} traces upon anti-CD3 stimulation (1 μg/ml). Right: Basal Ca^{2+} concentration, signal onset velocity, peak Ca^{2+} concentration, and plateau Ca^{2+} concentration. Data are means ± SEM from $n = 38$ (*Duox1*$^{-/-}$) or 71 (*Duox1*$^{-/-}$/BZ194) cells. Statistical analysis as in (B); *$P < 0.05$, **$P < 0.005$. (**D**) Comparison of DMSO-treated *Duox2*$^{-/-}$ versus BZ194-treated *Duox2*$^{-/-}$ T cells, treated as in (B). Left: Kinetics of mean Ca^{2+} traces upon anti-CD3 stimulation (1 μg/ml). Right: Basal Ca^{2+} concentration, signal onset velocity, peak Ca^{2+} concentration, and plateau Ca^{2+} concentration. Data are means ± SEM from $n = 84$ (*Duox2*$^{-/-}$) or 48 (*Duox2*$^{-/-}$/BZ194) cells. Statistical analysis as in (B).

(*3*)] (fig. S3). Reduction of NAADP to NAADPH by GLC-6-P-DH and lack of Ca^{2+} release activity of NAADPH were first described by Genazzani and co-workers (*15*). Under the reducing conditions present in the cytosol, an about 85- to 100-fold excess of the reduced form is likely, as for NADPH/NADP (*27*). Hence, we suggest a DUOX2- and GLC-6-P-DH–catalyzed redox cycle for production and degradation of NAADP through NAADPH as inactive intermediate (fig. S3) accounting for increased [NAADP] after TCR/CD3 stimulation (*3*).

Upon TCR/CD3 stimulation, rapid activation of DUOX2 is required. Cell-free and cell-based assays indicate that DUOX2 may work as coincidence detector, becoming activated by locally and temporarily coordinated increases in $[Ca^{2+}]_i$ and protein kinase C (PKC) activator diacylglycerol (DAG) (*28*). Spontaneous Ca^{2+}

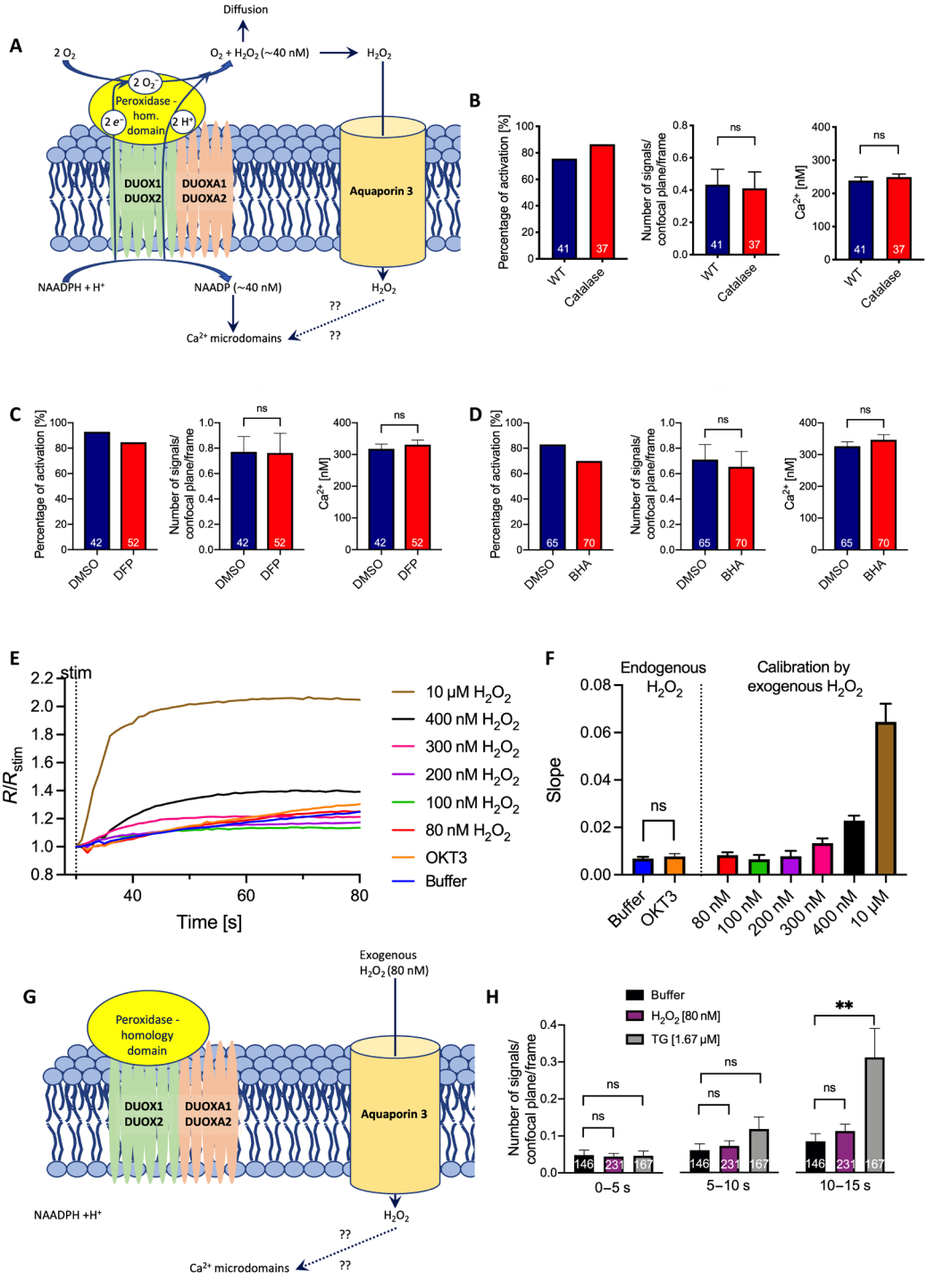

Fig. 7. Does the second product of NAADPH oxidation, H_2O_2, affect the formation of initial Ca^{2+} microdomains in CD4$^+$ effector T cells?ABCDE FGH (**A**) Scheme of NAADPH oxidation by DUOX1/2: NADPH binds at the intracellular portion of DUOX1/2, two electrons (e^-) are transferred to two O_2 and two O_2^- anions are intermediately generated. The latter further react in a dismutation reaction to O_2 and H_2O_2. Release of H_2O_2 proceeds to the extracellular space. Given that H_2O_2 cannot penetrate the plasma membrane, we assumed transport through aquaporin 3. (**B**) WT mouse CD4$^+$ T cells loaded with both Fluo4-AM and Fura-Red for high-resolution Ca^{2+} imaging were either untreated or incubated with catalase (1000 to 2500 U/ml) for 5 min and then stimulated by an anti-CD3/anti-CD28–coated bead. Statistical analysis across the first 15 s of stimulation was shown as percentage of activated cells, number of Ca^{2+}microdomains, and average Ca^{2+} concentration of the microdomains. Data are means ± SEM from $n = 41$ (WT) and 37 (WT per catalase) cells. ns, not significant by a nonparametric Mann-Whitney *U* test. (**C**) WT mouse CD4$^+$ T cells were treated either with vehicle DMSO or with aquaporin inhibitor DFP00173 (25 µM) for 10 min and then stimulated as in (B). Ca^{2+}signaling parameters were quantitatively and statistically analyzed as in (B). Data are means ± SEM from $n = 42$ (WT) and 52 (WT/DFP00173) cells. (**D**) WT mouse CD4$^+$ T cells were treated with either vehicle (DMSO) or ROS scavenger BHA (50 µM) for 5 min and then stimulated as in (B). Ca^{2+}signaling parameters and data were analyzed as in (B). Data are means ± SEM from $n = 65$ (WT) and 70 (WT/BHA) cells. (**E** and **F**) WT Jurkat T cells were transfected with HyPer7-MEM and stimulated after 30 s with buffer, OKT3 (1 µg/ml), or freshly diluted H_2O_2 as indicated. Mean tracings of the HyPer7-MEM ratio $488_{ex}/405_{ex}$ normalized to the time point of stimulation (R/R_{stim}) are shown in (E), and signal onset velocities of the tracings were calculated in (F). Data are means ± SEM from buffer, $n = 42$ cells; OKT3, $n = 40$ cells; 80 nM H_2O_2, $n = 36$ cells; 100 nM H_2O_2, $n = 16$ cells; 200 nM H_2O_2, $n = 18$ cells; 300 nM H_2O_2, $n = 37$ cells; 400 nM H_2O_2, $n = 43$ cells; and 10 µM H_2O_2, $n = 42$ cells. Statistical analysis as in (B). (**G**) Scheme of extracellular addition of H_2O_2. (**H**) WT T cells were incubated either with extracellular buffer (buffer), 80 nM H_2O_2 in buffer, or thapsigargin (TG; positive control) during analysis of Ca^{2+}microdomains. Ca^{2+}signaling parameters were analyzed as in (B). Data are means ± SEM from WT/buffer, $n = 146$ cells; WT/H_2O_2, $n = 231$ cells; and WT/TG, $n = 167$ cells. $^{**}P < 0.005$ by nonparametric Kruskal-Wallis test and Dunn's correction for multiple testing.

microdomains that occur even before TCR/CD3 stimulation in T cells (*2*) may act as one of the signals required for rapid activation of DUOX2.

In addition, sufficient GLC-6-P-DH activity is necessary to rapidly reduce NAADP to NAADPH to terminate initial activation of DUOX2. NAADP concentration 10 s after TCR/CD3 stimulation is 34 nM or 0.245 pmol/mg protein; it dropped back to almost basal level (about 0.101 pmol/mg protein) within the next 10 s (*3*), requiring a GLC-6-P-DH activity of about 0.864 pmol/min per milligram

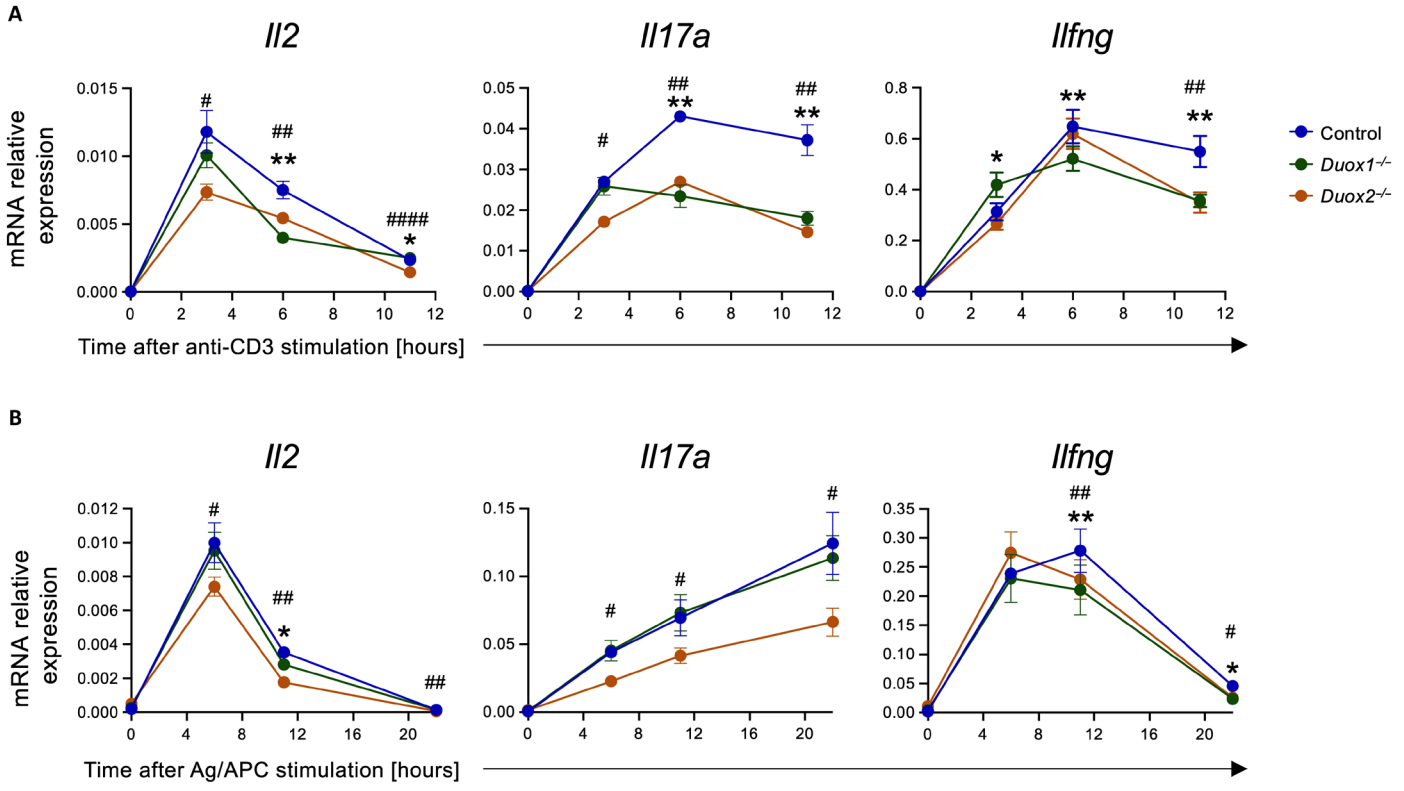

Fig. 8. Knockout of *Duox1* or *Duox2* differentially affects cytokine production in CD4$^+$ effector T cells. (**A** and **B**) Transcriptional response of rat effector T cells after stimulation with either (A) anti-CD3 antibodies (1 μg/ml) or (B) cognate antigen (Ag, myelin basic protein, 5 μg/ml) presented by thymic antigen-presenting cells (APCs). Data are means ± SEM of relative expression levels normalized to ß-actin expression determined by qPCR, from $n = 3$ independent experiments. Comparisons of control versus *Duox1*$^{-/-}$ cells (*$P < 0.05$ and **$P < 0.01$) and control versus *Duox2*$^{-/-}$ cells ($^{\#}P < 0.05$ and $^{\#\#}P < 0.01$) by repeated-measures one-way ANOVA with Tukey's multiple comparisons test.

protein. GLC-6-P-DH is expressed in T cells, and enzyme activity at saturation for substrate NADP was determined to be about 7.5 nmol/min per milligram protein (*29*). Further, at substrate saturation, we found an approximately 714-fold decreased activity for substrate NAADP over substrate NADP (Fig. 2D, right), resulting in an activity of about 10.5 pmol/min per milligram protein for NAADP-to-NAADPH conversion. However, the NAADP concentration 10 s after TCR/CD3 stimulation is 34 nM (*3*), thus far below the K_m of GLC-6-P-DH for NAADP, which is 2.3 μM (Fig. 2D and see Results). We used a linear approximation to estimate GLC-6-P-DH activity for NAADP at 34 nM, resulting in 0.155 pmol/min per milligram protein. This value is in the same range but somewhat lower as the activity necessary for rapid conversion of NAADP to NAADPH in the T cell (0.864 pmol/min per milligram protein). Therefore, this result confirms that GLC-6-P-DH activity level in T cells is compatible with the concept that GLC-6-P-DH rapidly converts NAADP to NAADPH in the low nanomolar range. The small discrepancy in the calculations may be because all enzyme assays were carried out in cell-free systems, perhaps with somewhat suboptimal conditions. Furthermore, we cannot exclude an activation mechanism of GLC-6-P-DH that accelerates its activity. GLC-6-P-DH was recently reported to supply sufficient NADPH for NOX/DUOX for the oxidative burst in neutrophils (*30*), demonstrating that a redox cycle as suggested in fig. S3 involving NOX/DUOX and GLC-6-P-DH exists in leukocytes (*30*).

As a potential limitation of our study, the second product of DUOX isozymes—H_2O_2—had to be considered, because H_2O_2 may on its own regulate Ca^{2+} signaling. H_2O_2 activates ion channels, e.g., transient receptor potential, subtype melastatin 2 (*31*), and inhibits sarcoplasmic/endoplasmic reticular Ca^{2+} ATPase (SERCA2) by sulfonylation [reviewed in (*32*)]. At high concentration of H_2O_2, both mechanisms increase $[Ca^{2+}]_i$ (*31*, *33*). However, the main argument against a stimulatory role for H_2O_2 in the Ca^{2+} signals observed in our study is the low concentrations, such as when unstimulated about 5 nM and upon TCR/CD3 stimulation not more than 40 nM (*3*). Thus, taking into account the dismutation reaction of conversion of the primary product of DUOX, O_2^-, to H_2O_2, an equimolar product concentration of about 40 nM H_2O_2 is expected (scheme in Fig. 7A). Accordingly, neither addition of extracellular catalase that degrades H_2O_2, nor inhibition of H_2O_2 transporting aquaporin 3, nor scavenging of H_2O_2 by BHA (*34*) altered Ca^{2+} microdomains. Further, even when using the ultrasensitive H_2O_2 sensor, HyPer7 (*24*), expressed below the plasma membrane, TCR/CD3 stimulation did not result in H_2O_2 production above background, confirming our calculation of the expected low H_2O_2 concentration. Together, the low nanomolar H_2O_2 concentration produced in parallel to NAADP does not affect T cell Ca^{2+} homeostasis.

NAADP has been termed "a universal Ca^{2+} trigger" that acts during initiation of Ca^{2+} signaling (*3*, *35*, *36*). The decrease in the number of Ca^{2+} microdomains in *Duox2*$^{-/-}$ T cells is comparable to knockout of *Ryr1* gene (*1*) or *Hn1l/Jpt2* gene that encodes the recently discovered NAADP binding protein (*4*) or to pharmacological inhibition of NAADP signaling (*2*). Further, NAADP signaling

affects D-*myo*-inositol 1,4,5-trisphospate receptor (IP_3R) by providing Ca^{2+} as coagonist for full stimulation [reviewed in (*37*)]. Because D-*myo*-inositol 1,4,5-trisphospate (IP_3) peaks at about 2 to 3 min after TCR/CD3 stimulation, the signal onset velocity of global Ca^{2+} signaling and the Ca^{2+} peak amplitude are decreased in the absence of NAADP-generated trigger Ca^{2+}, as demonstrated here for *Duox2*$^{-/-}$ T cells and as recently shown in *Hn1l*$^{-/-}$ T cells (*4*). The crucial role of DUOX2 was further substantiated by demonstrating that this phenotype in *Duox2*$^{-/-}$ T cells was not further decreased by NAADP antagonism. In contrast, in *Duox1*$^{-/-}$ T cells, Ca^{2+} microdomain numbers were almost unaffected. Further, NAADP antagonism slowed down initial global Ca^{2+} signaling in *Duox1*$^{-/-}$ T cells. Collectively, these data suggest DUOX2 as the missing enzyme producing NAADP in the initial phase of T cell activation.

In addition to the initial signaling phase, endogenous NAADP was also increased about three- to fourfold from 5 to 20 min after TCR/CD3 stimulation (*3*). *Duox2*$^{-/-}$ or *Duox1*$^{-/-}$ T cells were characterized by decreased Ca^{2+} plateau amplitudes, a phenotype that was not altered by NAADP antagonism, suggesting that also in the plateau phase, NAADP signaling contributes to store-operated Ca^{2+} entry (SOCE) (*6*). However, although *Duox2*$^{-/-}$ or *Duox1*$^{-/-}$ T cells do not much differ during the Ca^{2+} plateau phase, such as 280 to 730 s after TCR/CD3 stimulation, different mechanisms may underlie these similar phenotypes. Kwon *et al.* (*38*) reported that knockdown of DUOX1 abolished TCR/CD3-evoked generation of H_2O_2 within the first 15 min after stimulation. Further, DUOX1, but not DUOX2, coimmunoprecipitated with IP_3R1 (*38*). TCR/CD3-evoked global Ca^{2+} signaling upon knockdown of DUOX1 in that study (*38*) was very similar to the phenotype of *Duox1*$^{-/-}$ T cells in our experiments. According to Kwon *et al.* (*38*), H_2O_2 produced by DUOX1 inhibits SHP-2, thereby enhancing ZAP-70 activity and subsequently PLCγ1-catalyzed formation of IP_3. In conclusion, it is likely that DUOX1 enhances T cell Ca^{2+} signaling through inhibition of SHP-2, whereas DUOX2 forms NAADP both in the initial phase and in the sustained phase of T cell Ca^{2+} signaling.

MATERIALS AND METHODS

Reagents

Fura2-AM, Fluo4-AM, and Fura-Red-AM were obtained from Life Technologies. All dyes were dissolved in dimethyl sulfoxide (DMSO), divided into aliquots, and stored at −20°C until required for use. Anti-mouse CD3 monoclonal antibody (mAb), anti-mouse CD28 mAb, anti-rat CD3 mAb, and anti-rat CD28 mAb were obtained from BD Biosciences. NAADP was obtained from Biolog (Bremen, Germany), and sodium dithionite was obtained from the Department of Organic Chemistry (University of Hamburg, Germany). All other chemicals were from Sigma-Aldrich-Merck, Darmstadt, Germany. Commercially available enzymes used were human GLC-6-P-DH (Abcam, ab126671), yeast GLC-6-P-DH (Sigma-Aldrich-Merck, Darmstadt, Germany, #232-602-6), yeast 6-phosphogluconate dehydrogenase (Sigma-Aldrich-Merck, Darmstadt, Germany, # 9073-95-4), yeast isocitrate dehydrogenase (Leebio, #341-02), and chicken malate dehydrogenase (Sigma-Aldrich-Merck, Darmstadt, Germany, #9028-47-1).

Cell lines

HEK293 cells were stably transfected with the pcDNA3.1 vector containing human NOX5 (PMID: 14982937). HEK cells were transduced with either human DUOX1 and DUOXA1, or DUOX2 and DUOXA2 (PMID: 31330481). Cell lines were cultured at 37°C in air with 5% CO_2 in Dulbecco's modified Eagle's medium (DMEM) containing glucose (4.5 g/liter) supplemented with 10% fetal bovine serum, penicillin (100 U/ml), and streptomycin (100 μg/ml).

The Jurkat subclone JMP was cultured in RPMI 1640 medium supplemented with GlutaMax I, 25 mM Hepes, 7.5% newborn calf serum (v/v), and penicillin (100 U/ml)/streptomycin (100 μg/ml). The density of the cells was kept between 0.3×10^6 and 1.0×10^6/ml. They were cultured in spinner bottles at 37°C with 5% CO_2 in air.

Animal models and removal of spleens

NADPH oxidase knockout mice Nox1$^{y/-}$ mice were previously characterized; NOX1 deficiency protects from aortic dissection in response to angiotensin II (*39*). Nox2$^{-/-}$ (B6.129S-Cybb^{tm1Din}/J) were purchased from the Jackson Laboratory. Breeding was performed by crossing homozygote *Nox1*$^{-/-}$ or *Nox2*$^{-/-}$ females with WT males, giving rise to either WT $^{(+/+)}$ or KO $^{(y/-)}$ male littermates. Mice were housed in a specific pathogen–free facility with 12-hour day/12-hour night cycle and free access to water and chow every time. Animals were euthanized by cervical dislocation, and spleen and lymph nodes were removed and shipped on ice in DMEM.

Duoxa1$^{-/-}$/*Duoxa2*$^{-/-}$ (*19*, *20*) and gender-matched WT littermates on C57BL6/J genetic background were cohoused (three to five animals per cage) in microisolator cages under specific pathogen–free conditions. Food and water were supplied ad libitum, with the latter including a supplemental dose of L-thyroxine to equalize thyroid hormone status. All animal studies were approved by the University of Michigan Institutional Animal Care and Use Committee (PRO-00007922). Spleens were collected after isoflurane overdose and shipped on ice in DMEM.

Cd38$^{-/-}$ mice (B6.129P2-*Cd38*^{tm1Lnd}/J) (*40*) and WT C57BL/6 were bred in the animal facility of the University Medical Center Hamburg-Eppendorf. Mice were housed under specific pathogen–free conditions with food and water ad libitum. Animal studies were approved by the local committee for animal experiments of the City of Hamburg (registration nos. 48/14, 55/19, and ORG727). Spleens and lymph nodes were dissected from mice, and T cells were purified as described below.

Targeting Duox1 or Duox2 in rat effector CD4 T cells

Retroviral short guide RNA expression constructs were cloned using modified pMSCV vector (Clontech) pMPuChe-U6zero as a backbone. There, long terminal repeat (LTR) promoter drives expression of puromycin resistance gene fused via 2A-like sequence to red fluorescent protein mCherry and followed by U6 promoter driving expression of crRNA. Four oligonucleotides, 5′-caccGCATCCCAAAAAGGAGGATCC-3′ and 5′-aaacGGATCCTCCTTTTTGGGATGC-3′ (Microsynth Seqlab, targeting CCTGGATCCTCCTTTTTGGGATG protospacer in the exon 2 of rat *Duox1* gene) and 5′-caccGTCCAGTCAACAGAGCGCCC-3′ and 5′-aaacGGGCGCTCTGTTGACTGGAC-3′ (Microsynth Seqlab, targeting CCTGGGCGCTCTGTTGACTGGAC protospacer in the exon 3 of rat *Duox2* gene), were annealed and ligated into Bbs I digested vector. Control short guide RNA was designed to target intronic sequence in the rat *Rosa26* locus (CCAGTGATACCCAGAGAAACCCT). Linearized plasmid DNA was transfected using Lipofectamine 3000 (Thermo Fisher Scientific) into GP+E86 ecotropic packaging cell line. After a 7-day selection in medium containing puromycin (1 μg/ml; Carl Roth), survivor packaging cells were sorted by flow cytometry and subcloned by

limiting dilution. Clones producing high titer of retroviruses were identified by short-term coculture with murine thymoma cell line BW5147 and flow cytometry analysis, expanded, and then used for T cell transduction. Effector T cell lines specific for ovalbumin or myelin basic protein (CD4-positive, mixed T_H1/T_H17 phenotype) were established as described previously (*41*) on a transgenic background ubiquitously expressing Cas9 nuclease. After two rounds of restimulation in culture, more than 95% of cells were Cherry positive, as determined by flow cytometry.

Isolation of primary murine T cells

Spleens and lymph nodes were dissected from mice and kept in cold medium until T cell isolation. Some spleens and lymph nodes were shipped to Hamburg, Germany, on wet ice. Murine $CD4^+$ T cells were isolated by negative selection using the EasySep Mouse $CD4^+$ T Cell Enrichment Kit (STEMCELL Technologies Inc.). Cell purity was typically 95% $CD4^+$ T cells and was determined by immunostaining with fluorescein isothiocyanate–conjugated anti-mouse TCRβ antibody (clone H57-597, BioLegend) and measured with a FACSCalibur flow cytometer (BD Biosciences).

Imaging of global Ca^{2+} signaling in primary T cells from mice or effector T cells from rats

Freshly isolated murine $CD4^+$ T cells or restimulated rat T cells were loaded with the membrane-permeable AM ester of Fura-2 (4 μM) for 30 min at 37°C in RPMI medium (mice) or DMEM medium (rats). After 15 min, 2 ml of fresh medium was added. The cells were rinsed twice and resuspended in Ca^{2+} buffer [140 mM NaCl, 5 mM KCl, 1 mM $MgSO_4$, 1 mM $CaCl_2$, 20 mM Hepes (pH 7.4), 1 mM NaH_2PO_4, and 5 mM glucose] and then kept for 20 min at room temperature (RT) for de-esterification. Cells were added on prepared coverslips, coated with bovine serum albumin (5 mg/ml; Sigma-Aldrich) and poly-L-lysine (0.1 mg/ml; Sigma-Aldrich), and allowed to adhere before measurement.

Cells were stimulated by anti-CD3 antibody (1 μg/ml) at 2 min, and 1.67 μM thapsigargin TG (Merck, Germany) was added at 15 min as a positive control. Cells were preincubated for 5 min with catalase (1000 to 2500 U/ml; control with equal volume Ca^{2+} buffer) or 5 min with 50 μM BHA (Sigma-Aldrich-Merck, Germany) and 10 min with 25 μM DFP00173 (Axon Medchem) [control with 0.5% (v/v) DMSO] at RT on coverslips, or with 500 μM NAADP antagonist BZ194 [control with 1% (v/v) DMSO] overnight at 37°C and 5% CO_2 in air in a humidified cell incubator.

Imaging was performed on a Leica IRBE microscope with 40-fold magnification. A Sutter DG-4 was used as a light source, and frames were acquired with an electron-multiplying charge-coupled device camera (Hamamatsu). One frame every 2 s was acquired using a Fura-2 filter set [excitation (ex), HC 340/26 nm, HC 387/11 nm; beam splitter (bs), 400DCLP; emission (em), 510/84 nm; AHF Analysentechnik]. $[Ca^{2+}]_i$ was determined either in Fura-2–loaded murine $CD4^+$ T cells or in restimulated rat T cells. Therefore, R_{min} [using the lowest ratio (R) and fluorescence (F) after EGTA chelation] and R_{max} (using the highest R and F after ionomycin incubation) of Fura-2 in single-cell measurements were assessed.

Imaging of initial Ca^{2+} microdomains after processing and analysis

Identification of local Ca^{2+} microdomains, image processing, calibration, and comparison for subcellular compartments were done as described in detail in (*42*). Briefly, freshly isolated murine $CD4^+$ T cells or restimulated rat T cells were loaded with Fluo4-AM (10 μM) and Fura-Red (20 μM) for 50 min at RT. To stimulate the T cells, protein G beads (Merck Millipore) were coated with antibodies (anti-CD3/anti-CD28). Cells were preincubated for 5 min with catalase (1000 to 2500 U/ml; control with equal volume Ca^{2+} buffer) or 5 min with 50 μM BHA and 10 min with 25 μM DFP00173 [control with 0.5% (v/v) DMSO] at RT on coverslips, or with 500 μM NAADP antagonist BZ194 (control with 1% DMSO) overnight at 37°C and 5% CO_2 in air in a humidified cell incubator. Commercially available H_2O_2 (10 M) was diluted with commercially available pure water into 50 μM stock solution and then diluted into 0.8 μM stock solution with Ca^{2+} buffer. The H_2O_2 stock solution was prepared freshly before the measurement and stored on ice. Imaging was carried out with an exposure time of 25 ms (40 frames/s) in a 14-bit mode using a dual-view module (Optical Insights, PerkinElmer Inc.) to split the emission wavelengths [filters: ex, 480/40; bs, 495; emission 1 (em1) 1, 542/50; em2, 650/57]. For Ca^{2+} microdomain detection in cell images, all pixel $[Ca^{2+}]_i$ values of the microdomain had to be at least $\Delta[Ca^{2+}]_i$ = 90 nM higher than the frame-specific mean $[Ca^{2+}]_i$ of the considered cell. For the comparison of subcellular compartments, a so-called "dartboard projection" approach was introduced. Here, a circular, dartboard-like template was matched onto every individual cell. On the basis of their spatial coordinates, the identified local Ca^{2+} signals were assigned to the corresponding dartboard. Every individual dartboard was normalized with respect to the location of the stimulating bead by rotation. In the last step, the dartboard information for all individual cells was aggregated and evaluated.

Expression of NOX/DUOX

Total RNA was isolated from T cells isolated from spleen using a NucleoSpin RNA II kit (Macherey-Nagel). After synthesis of complementary DNA (cDNA), quantitative real-time polymerase chain reaction (PCR) was performed, and the relative expression of genes of interest was calculated by normalization to housekeeper TATA box–binding protein (Tbp) as described (*43*). The following TaqMan Assay-on-Demand primer sets (Applied Biosystems) were used—cytochrome b-245, beta polypeptide (*Cybb*, also known as *Nox2*): Mm01287743_m1; dual oxidase 1 (*Duox1*): Mm01328685_m1; dual oxidase 2 (*Duox2*): Mm01326247_m1; NADPH oxidase 1 (*Nox1*): Mm00549170_m1; NADPH oxidase 3 (*Nox3*): Mm01339132_m1; and NADPH oxidase 4 (*Nox4*): Mm00479246_m1; *Tbp*: Mm00446973_m1. Expression data for the respective mouse and rat genes were extracted from RNA-sequencing datasets described in (*44*) and (*45*), respectively.

Chemical and enzymatic preparation of NAADPH

Production of reduced NAADP was performed as previously described (*15*). NAADP (3.72 μmol) was dissolved in 1 ml of buffer containing 400 mM $NaHCO_3$ and 115 mM sodium dithionite. The solution was incubated in the dark for 2 hours under a constant flow of argon. After 2 hours, the solution was loaded onto a HiTrap DEAE FF 1-ml column, equilibrated with 20 mM Hepes (pH 8.0), using a peristaltic pump at a flow rate of 1 ml/min. NAADPH was then eluted using a linear gradient from 0 to 300 mM NaCl. NAADPH usually eluted in the range between 120 and 150 mM NaCl. Fractions of 1 ml were collected and analyzed for absorption at 260 and 340 nm using a NanoDrop photometer. The fractions with the highest

absorption at 340 nm were pooled and immediately aliquoted. The single aliquots were treated with argon and kept at −80°C until use. The quality and quantity of each batch were controlled by HPLC (Agilent, 1260 Infinity and 1200 Infinity) using a BDS Multohyp 5µ column (250 × 4.6 mm) and buffer A [20 mM KH_2PO_4, 14.7 mM tetrabutylammoniumphosphate (TBAP)] and buffer B [50% (v/v) HPLC-Puffer A, 50% (v/v) methanol]. Gradient was 0 to 3.5 min 30% B, 3.5 to 11 min linear increase to 62.5% B, 11 to 15 min 62.5% B, 15 to 25 min linear increase to 100% B, 25 to 27 min linear decrease to 30% B, and re-equilibration from 29 to 38 min at 30% B. The amount of NAADPH was determined by an NADPH standard at 340 nm because of the almost identical absorption at that wavelength [NAADPH 6228 1/cm*M and NADPH 6220 1/cm*M; (*15*)].

Enzyme assays and HPLC of nucleotides

Membranes from NOX5-overexpressing HEK293 cells were obtained and used as follows. After cell homogenization using an Elvehjem-Potter homogenizer, cell lysate was centrifuged stepwise using the supernatant for the next step as indicated: at 500*g* for 15 min (Heraeus Varifuge), at 2000*g* for 10 min (Heraeus Varifuge), at 10,000*g* for 30 min (Sorvall RC6plus), and, last, at 100,000*g* for 90 min (Ultracentrifuge L7-80). During the whole procedure, the cell lysate or supernatant was kept at 4°C. The final pellet contains the P100 membranes and was dissolved in 20 mM Hepes (pH 7.4) supplemented with cOmplete, Mini, EDTA-free Protease Inhibitor Cocktail (Roche), aliquoted, quantified by Bio-Rad protein assay, and stored at −80°C until use. Enzyme assay was conducted in 50 mM Hepes buffer (pH 7.4), 5.5 µM phosphatidic acid, 10 µM flavin adenine dinucleotide (FAD), 450 µM tris(carboxymethyl)amine (NTA), 450 µM EDTA, 1 mM $MgCl_2$, 700 µM $CaCl_2$, P100 membranes (10 µg protein/ml), and varying concentrations of NADPH or NAADPH. For estimation of the pH dependency of NOX5, the following buffers were used: 50 mM acetate buffer (pH 5.0 to 5.5), 50 mM MES buffer (pH 6.0 to 6.5), 50 mM Hepes buffer (pH 7.0 to8.0), and 50 mM tris buffer (pH 8.5 to 9.0).

After homogenization, HEK cell membranes overexpressing DUOX1 or DUOX2 were purified by ultracentrifugation in a sucrose gradient as described in detail (*46*). Protein concentration was determined with Bradford reagent using BSA as a standard. Aliquots were kept at −80°C and shipped in dry ice. Enzyme assay was conducted in 50 mM Hepes buffer (pH 7.1), 5.5 µM phosphatidic acid, 10 µM FAD, 450 µM tris(carboxymethyl)amine (NTA), 450 µM EDTA, 1 mM $MgCl_2$, 1.4 mM $CaCl_2$, DUOX1/DUOX2 membranes (250 µg protein/ml), and 50 µM NADPH or NAADPH.

Jurkat JMP membranes were isolated as described in (*47*). Briefly, cells were homogenized, ultracentrifuged in a sucrose gradient (11, 17, and 40%), and the membrane fraction was isolated. Protein concentration was determined using the standard Bradford procedure (Sigma-Aldrich), and the membrane fraction was stored at −80°C until use.

For the enzyme assay, the membranes (1 mg protein/ml) were preincubated for 10 min with either vehicle DMSO or, for negative controls, with 5 µM NOX/DUOX inhibitor diphenyleniodonium-chloride (DPI) (Merck). Then, the reaction buffer containing 50 µM NAADPH, 5.5 µM phosphatidic acid (Cayman Chemical), 1.4 mM $CaCl_2$, 1 mM $MgCl_2$, 450 µM NTA (Honeywell), 450 µM EDTA, 10 µM FAD (Sigma-Aldrich), and 50 mM Hepes at pH 7.1 was added; in negative controls, FAD was not included. The incubation was conducted at 37°C for different periods of time. Then, samples were transferred on ice, and proteins were quickly removed by passing samples through Nanosep filtration tubes (PALL, 10 kDa cutoff; 10 min at 10,000*g* and 4°C). Last, the samples were immediately frozen in liquid nitrogen, stored at −80°C, and thawed directly before HPLC analysis. The reaction products were analyzed on HPLC (Agilent Technologies, 1200) with a C8 column [Phenomenex Luna 5u C8(2) 100A (250 × 4.60 mm, particle size 5 µm)] equipped with a guard cartridge (4 mm × 3.0 mm), containing a C8 filter element (Phenomenex). Analyses were done at a flow rate of 0.8 ml/min with a linear gradient of methanol in the running buffer (20 mM KH_2PO_4 and pH 6.0). The methanol gradient was 0 min (0%), 5 min (0%), 27.5 min (50%), 30 min (50%), 32 min (0%), and 43 min (0%). The diode array detector (Agilent Technologies) was set to 260 nm (for all nucleotides) and 340 nm (for reduced nucleotides). For peak integration, the ChemStation Software (Rev. C.01.05, Agilent Technologies) was used. Each product was quantified using standards on the HPLC, and enzyme activity at different time points was calculated by subtracting the amount in corresponding negative control samples.

Human GLC-6-P-DH (6.68 pkat/ml) or other dehydrogenases (8.35 nkat/ml) of enzyme were used in 50 mM phosphate buffer (pH 7.4) and 10 µM NADP or NAADP, if not otherwise specified. Product formation was analyzed photometrically in a microplate reader at 340 nm for 10 min (Tecan Infinity 200; acquisition interval: 30s, bandwidth: 9 nm, and number of lightning: 25).

STED super-resolution microscopy

Primary T cells were seeded on slides that were coated with poly-L-lysine (0.1 mg/ml) and fixed with 4% (w/v) para-formaldehyde (Alfa Aesar) for 15 min. In addition, the permeabilization was done with 0.05% (w/v) saponin (Fluka) for 15 min. To block unspecific binding sites, cells were incubated with 10% (v/v) fetal bovine serum overnight at 4°C. Primary antibodies [rabbit anti-DUOX1, 1:100 (orb156652, Biorbyt) or rabbit anti-DUOX2, 1:100 (NB110-61576, Novusbio)] were diluted in 3% (v/v) fetal bovine serum, and the incubation was done for 1 hour at RT. The secondary antibody (anti-rabbit Alexa Fluor 594, 1:200; A11037, BioLegend) was diluted in 3% (v/v) fetal bovine serum and incubated for 1 hour at RT. Coverslips were mounted with Abberior Mount Solid (Abberior) overnight at 4°C. To acquire images, the Abberior Expert Line four-channel EASY3D STED equipped with a depletion beam (Abberior Instruments), a Nikon 60×, 1.4–numerical aperture objective, and a QUAD beam scanner were used. Alexa Fluor 594 was excited with a pulsed 561-nm diode beam, depleted with a pulsed 775-nm STED beam and detected with a 615 ± 20–nm emission filter.

Validation of antibody specificity

To test the specificity of the antibodies used for the STED experiments, WT, *Duox1*$^{-/-}$, or *Duox2*$^{-/-}$ rat T cells were fixed and stained as described above. In this experiment, in contrast, we used anti-rabbit Alexa Fluor 488 (1:400; A21206, Life Technologies) and anti-mouse Alexa Fluor 568 (1:400; A11004, Thermo Fisher Scientific) as secondary antibodies and incubated for 1 hour at RT. Furthermore, the nuclei were stained by incubation with 4′,6-diamidino-2-phenylindole (DAPI) (62247, Thermo Fisher Scientific; 1:1000) for 10 min at RT. Images were acquired using a super-resolution spinning-disk imaging system (Visitron) equipped with a ×100 magnification objective (Zeiss) and a scientific complementary metal oxide semiconductor (sCMOS) camera (Orca-Flash 4.0, C13440-20CU,

Hamamatsu). The following lasers and filters were used for the respective dyes and fluorophores—DAPI: ex, 405 nm laser; em filter, 460/50 nm; Alexa Fluor 488: ex, 488 nm laser; em, 525/50 nm; and Alexa Fluor 568: ex, 561 nm laser; em, 609/54 nm.

Determination of endogenous H_2O_2 using HyPer7 sensor

To analyze endogenous H_2O_2, 2×10^6 WT Jurkat T cells were transfected with 5 μg of HyPer7-MEM (*24*) by electroporation using the Neon Transfection System (Invitrogen) according to the manufacturer's instructions. The pCMV-HyPer7-MEM vector was a gift from V. Belousov (Addgene, plasmid no. 136465; http://n2t.net/addgene:136465; RRID: Addgene_136465). Before transfection, the cells were washed in phosphate-buffered saline (without Ca^{2+} and Mg^{2+}) and resuspended in 100 μl of resuspension buffer R [a proprietary buffer of the Neon Transfection System (Invitrogen)]. Electroporation was performed with two 1400-V pulses for 20 ms. After electroporation, cells were cultured overnight. For image acquisition, cells were seeded on coverslips, and images were acquired with a spinning-disk confocal imaging system (Visitron) at 100-fold magnification. Fluorescence of HyPer7-MEM was excited sequentially with 405-m and 488-nm lasers for 400 ms with 40% laser power. The emission for both lasers was collected using 525/50 emission filter in front of a sCMOS camera (Orca-Flash 4.0, C13440-20CU, Hamamatsu). After 30 s, either OKT3 (1 μg/ml), buffer, or the respective H_2O_2 concentrations (final concentrations 80 nM, 200 nM, 300 nM, 400 nM, and 10 μM) were added. For the analysis, a background correction was performed before calculating the ratio $488_{ex}/405_{ex}$ and normalizing the ratio to the time point of stimulation (R/R_{stim}).

Cytokine expression in Duox1$^{-/-}$ and Duox2$^{-/-}$ T cells

Resting T cells were seeded as triplicates in 96-well plates in a 50-μl volume of DMEM-based T cell medium supplemented with 1% rat serum (*41*) at a density of 1×10^5 per well. Anti-CD3 antibodies (clone G4.18, BD Biosciences) were added in a 50-μl volume of restimulation medium to a final concentration of 1 μg/ml. In parallel, a suspension of 2×10^6 per well Lewis thymocytes, irradiated at a dose of 30 Gy, in restimulation medium in the presence of cognate antigen (myelin basic protein; final concentration, 5 μg/ml) was added. Total RNA was isolated from T cell pellets collected by centrifugation using an RNeasy miniprep kit (Qiagen) as per the manufacturer's instructions and reversely transcribed using random hexamer priming and FirstAid First-Strand cDNA synthesis kit (Thermo Fisher Scientific). PCR amplification was carried out using quantitative PCR (qPCR) master mix (Eurogentec) on a StepOne Plus real-time PCR system (Applied Biosystems). Rat β-actin (*Bact*) served as a housekeeping gene.

The primers and probes (Sigma-Aldrich) used for the detection of rat genes were as follows: *Bact* (Fw: 5′-GTA CAA CCT CCT TGC AGC TCC T-3′, Rev: 5′-TTG TCG ACG ACG AGC GC-3′, probe: 5′-Fam-CGC CAC CAG TTC GCC ATG GAT-Tamra-3′), *Ifng* (Fw: 5′-AAC AGT AAA GCA AAA AAG GAT GCA TT-3′, Rev: 5′-TTC ATT GAC AGC TTT GTG CTG G-3′, probe: 5′-Fam-CGC CAA GTT CGA GGT GAA CAA CCC -Tamra-3′), *Il2* (Fw: 5′-CTC CCC ATG ATG CTC ACG TT-3′, Rev: 5′-TCA TTT TCC AGG CAC TGA AGA TG-3′, probe: 5′-Fam-CAA TTC TGT GGC CTG CTT GG-Tamra-3′), and *Il17a* (Fw: 5′-GAG TCC CCG GAG AAT TCC AT-3′, Rev: 5′-GAG TAC CGC TGC CTT CAC TGT-3′, probe: 5′-Fam-ATG TGC CTG ATG CTG TT-Tamra-3′).

Statistical analysis

Data analysis was performed with Prism 7 and 8 (GraphPad Software, USA). All data are shown as means ± SEM of at least three independent experiments. No specific randomization or blinding protocols were used. Datasets were tested for normal distribution by Kolmogorov-Smirnov test with Dallal-Wilkinson-Lillie for *P* value. Not normally distributed data were tested with a nonparametric Mann-Whitney *U* test or a Kruskal-Wallis test with subsequent Dunn's correction for multiple testing using Prism 8. K_m and V_{max} values of G6PDH and NOX5 were estimated by nonlinear fitting using Prism 7. Gene expression values on WT, *Duox1*$^{-/-}$, and *Duox2*$^{-/-}$ were calculated by repeated-measures one-way analysis of variance (ANOVA) with Tukey's multiple comparisons test in Prism 8. Differences with a *P* value of <0.05 were considered statistically significant: *$P < 0.05$; **$P < 0.005$; ***$P < 0.001$; ****$P < 0.0001$.

SUPPLEMENTARY MATERIALS

www.science.org/doi/10.1126/scisignal.abe3800
Figs. S1 to S7

View/request a protocol for this paper from *Bio-protocol*.

REFERENCES AND NOTES

1. I. M. A. Wolf, B.-P. Diercks, E. Gattkowski, F. Czarniak, J. Kempski, R. Werner, D. Schetelig, H.-W. Mittrücker, V. Schumacher, M. von Osten, D. Lodygin, A. Flügel, R. Fliegert, A. H. Guse, Frontrunners of T cell activation: Initial, localized Ca^{2+} signals mediated by NAADP and the type 1 ryanodine receptor. *Sci. Signal.* **8**, ra102 (2015).
2. B.-P. Diercks, R. Werner, P. Weidemüller, F. Czarniak, L. Hernandez, C. Lehmann, A. Rosche, A. Krüger, U. Kaufmann, M. Vaeth, A. V. Failla, B. Zobiak, F. I. Kandil, D. Schetelig, A. Ruthenbeck, C. Meier, D. Lodygin, A. Flügel, D. Ren, I. M. A. Wolf, S. Feske, A. H. Guse, ORAI1, STIM1/2, and RYR1 shape subsecond Ca^{2+} microdomains upon T cell activation. *Sci. Signal.* **11**, eaat0358 (2018).
3. A. Gasser, S. Bruhn, A. H. Guse, Second messenger function of nicotinic acid adenine dinucleotide phosphate revealed by an improved enzymatic cycling assay. *J. Biol. Chem.* **281**, 16906–16913 (2006).
4. H. G. Roggenkamp, I. Khansahib, L. C. H. C. Y. Zhang, D. Lodygin, A. Krüger, F. Gu, F. Möckl, A. Löhndorf, V. Wolters, D. Woike, A. Rosche, A. Bauche, D. Schetelig, R. Werner, H. Schlüter, A. V. Failla, C. Meier, R. Fliegert, T. F. Walseth, A. Flügel, B.-P. Diercks, A. H. Guse, HN1L/JPT2: A signaling protein that connects NAADP generation to Ca^{2+} microdomain formation. *Sci. Signal.* **14**, eabd5647 (2021).
5. G. S. Gunaratne, E. Brailoiu, S. He, E. M. Unterwald, S. Patel, J. T. Slama, T. F. Walseth, J. S. Marchant, Essential requirement for JPT2 in NAADP-evoked Ca^{2+} signaling. *Sci. Signal.* **14**, eabd5605 (2021).
6. M. F. Langhorst, N. Schwarzmann, A. H. Guse, Ca^{2+} release via ryanodine receptors and Ca^{2+} entry: Major mechanisms in NAADP-mediated Ca^{2+} signaling in T-lymphocytes. *Cell. Signal.* **16**, 1283–1289 (2004).
7. W. Dammermann, A. H. Guse, Functional ryanodine receptor expression is required for NAADP-mediated local Ca^{2+} signaling in T-lymphocytes. *J. Biol. Chem.* **280**, 21394–21399 (2005).
8. M. Steen, T. Kirchberger, A. H. Guse, NAADP mobilizes calcium from the endoplasmic reticular Ca^{2+} store in T-lymphocytes. *J. Biol. Chem.* **282**, 18864–18871 (2007).
9. W. Dammermann, B. Zhang, M. Nebel, C. Cordiglieri, F. Odoardi, T. Kirchberger, N. Kawakami, J. Dowden, F. Schmid, K. Dornmair, M. Hohenegger, A. Flügel, A. H. Guse, B. V. L. Potter, NAADP-mediated Ca^{2+} signaling via type 1 ryanodine receptor in T cells revealed by a synthetic NAADP antagonist. *Proc. Natl. Acad. Sci. U.S.A.* **106**, 10678–10683 (2009).
10. C. Cordiglieri, F. Odoardi, B. Zhang, M. Nebel, N. Kawakami, W. E. F. Klinkert, D. Lodygin, F. Lühder, E. Breunig, D. Schild, V. K. Ulaganathan, K. Dornmair, W. Dammermann, B. V. L. Potter, A. H. Guse, A. Flügel, Nicotinic acid adenine dinucleotide phosphate-mediated calcium signalling in effector T cells regulates autoimmunity of the central nervous system. *Brain* **133**, 1930–1943 (2010).
11. R. Aarhus, R. M. Graeff, D. M. Dickey, T. F. Walseth, H. C. Lee, ADP-ribosyl cyclase and CD38 catalyze the synthesis of a calcium-mobilizing metabolite from $NADP^+$. *J. Biol. Chem.* **270**, 30327–30333 (1995).
12. F. Schmid, S. Bruhn, K. Weber, H.-W. Mittrücker, A. H. Guse, CD38: A NAADP degrading enzyme. *FEBS Lett.* **585**, 3544–3548 (2011).
13. S. Bruzzone, S. Kunerth, E. Zocchi, A. De Flora, A. H. Guse, Spatio-temporal propagation of Ca^{2+} signals by cyclic ADP-ribose in 3T3 cells stimulated via purinergic P2Y receptors. *J. Cell Biol.* **163**, 837–845 (2003).

14. S. Soares, M. Thompson, T. White, A. Isbell, M. Yamasaki, Y. Prakash, F. E. Lund, A. Galione, E. N. Chini, NAADP as a second messenger: Neither CD38 nor base-exchange reaction are necessary for in vivo generation of NAADP in myometrial cells. *Am. J. Physiol. Cell Physiol.* **292**, C227–C239 (2007).
15. R. A. Billington, J. W. Thuring, S. J. Conway, L. Packman, A. B. Holmes, A. A. Genazzani, Production and characterization of reduced NAADP (nicotinic acid-adenine dinucleotide phosphate). *Biochem. J.* **378**, 275–280 (2004).
16. K. Essuman, D. W. Summers, Y. Sasaki, X. Mao, A. DiAntonio, J. Milbrandt, The SARM1 Toll/interleukin-1 receptor domain possesses intrinsic NAD^+ cleavage activity that promotes pathological axonal degeneration. *Neuron* **93**, 1334–1343.e5 (2017).
17. K. Essuman, D. W. Summers, Y. Sasaki, X. Mao, A. K. Y. Yim, A. DiAntonio, J. Milbrandt, TIR domain proteins are an ancient family of NAD^+-consuming enzymes. *Curr. Biol.* **28**, 421–430.e4 (2018).
18. Z. Y. Zhao, X. J. Xie, W. H. Li, J. Liu, Z. Chen, B. Zhang, T. Li, S. L. Li, J. G. Lu, L. Zhang, L.-H. Zhang, Z. Xu, H. C. Lee, Y. J. Zhao, A cell-permeant mimetic of NMN activates SARM1 to produce cyclic ADP-ribose and induce non-apoptotic cell death. *iScience* **15**, 452–466 (2019).
19. H. Grasberger, S. Refetoff, Identification of the maturation factor for dual oxidase. Evolution of an eukaryotic operon equivalent. *J. Biol. Chem.* **281**, 18269–18272 (2006).
20. H. Grasberger, X. De Deken, O. B. Mayo, H. Raad, M. Weiss, X.-H. Liao, S. Refetoff, Mice deficient in dual oxidase maturation factors are severely hypothyroid. *Mol. Endocrinol.* **26**, 481–492 (2012).
21. G. P. Bienert, F. Chaumont, Aquaporin-facilitated transmembrane diffusion of hydrogen peroxide. *Biochim. Biophys. Acta* **1840**, 1596–1604 (2014).
22. I. V. da Silva, G. Soveral, Aquaporins in immune cells and inflammation: New targets for drug development. *Int. J. Mol. Sci.* **22**, 1845 (2021).
23. Y. Sonntag, P. Gena, A. Maggio, T. Singh, I. Artner, M. K. Oklinski, U. Johanson, P. Kjellbom, J. D. Nieland, S. Nielsen, G. Calamita, M. Rützler, Identification and characterization of potent and selective aquaporin-3 and aquaporin-7 inhibitors. *J. Biol. Chem.* **294**, 7377–7387 (2019).
24. V. V. Pak, D. Ezeriņa, O. G. Lyublinskaya, B. Pedre, P. A. Tyurin-Kuzmin, N. M. Mishina, M. Thauvin, D. Young, K. Wahni, S. A. Martínez Gache, A. D. Demidovich, Y. G. Ermakova, Y. D. Maslova, A. G. Shokhina, E. Eroglu, D. S. Bilan, I. Bogeski, T. Michel, S. Vriz, J. Messens, V. V. Belousov, Ultrasensitive genetically encoded indicator for hydrogen peroxide identifies roles for the oxidant in cell migration and mitochondrial function. *Cell Metab.* **31**, 642–653.e6 (2020).
25. H. C. Lee, R. Aarhus, A derivative of NADP mobilizes calcium stores insensitive to inositol trisphosphate and cyclic ADP-ribose. *J. Biol. Chem.* **270**, 2152–2157 (1995).
26. C. Fang, T. Li, Y. Li, G. J. Xu, Q. W. Deng, Y. J. Chen, Y. N. Hou, H. C. Lee, Y. J. Zhao, CD38 produces nicotinic acid adenosine dinucleotide phosphate in the lysosome. *J. Biol. Chem.* **293**, 8151–8160 (2018).
27. R. L. Veech, L. V. Eggleston, H. A. Krebs, The redox state of free nicotinamide-adenine dinucleotide phosphate in the cytoplasm of rat liver. *Biochem. J.* **115**, 609–619 (1969).
28. S. Rigutto, C. Hoste, H. Grasberger, M. Milenkovic, D. Communi, J. E. Dumont, B. Corvilain, F. Miot, X. D. Deken, Activation of dual oxidases Duox1 and Duox2: Differential regulation mediated by cAMP-dependent protein kinase and protein kinase C-dependent phosphorylation. *J. Biol. Chem.* **284**, 6725–6734 (2009).
29. M. Al-Essa, G. S. Dhaunsi, W. Al-Qabandi, I. Khan, Impaired NADPH oxidase activity in peripheral blood lymphocytes of galactosemia patients. *Exp. Biol. Med.* **238**, 779–786 (2013).
30. J. M. Ghergurovich, J. C. García-Cañaveras, J. Wang, E. Schmidt, Z. Zhang, T. TeSlaa, H. Patel, L. Chen, E. C. Britt, M. Piqueras-Nebot, M. C. Gomez-Cabrera, A. Lahoz, J. Fan, U. H. Beier, H. Kim, J. D. Rabinowitz, A small molecule G6PD inhibitor reveals immune dependence on pentose phosphate pathway. *Nat. Chem. Biol.* **16**, 731–739 (2020).
31. E. Wehage, J. Eisfeld, I. Heiner, E. Jüngling, C. Zitt, A. Lückhoff, Activation of the cation channel long transient receptor potential channel 2 (LTRPC2) by hydrogen peroxide. A splice variant reveals a mode of activation independent of ADP-ribose. *J. Biol. Chem.* **277**, 23150–23156 (2002).
32. J. M. Roscoe, C. S. Sevier, Pathways for sensing and responding to hydrogen peroxide at the endoplasmic reticulum. *Cell* **9**, 2314 (2020).
33. E. Schröder, P. Eaton, Hydrogen peroxide as an endogenous mediator and exogenous tool in cardiovascular research: Issues and considerations. *Curr. Opin. Pharmacol.* **8**, 153–159 (2008).
34. G. H. Hwang, Y. J. Jeon, H. J. Han, S. H. Park, K. M. Baek, W. Chang, J. S. Kim, L. K. Kim, Y.-M. Lee, S. Lee, J.-S. Bae, J.-G. Jee, M. Y. Lee, Protective effect of butylated hydroxylanisole against hydrogen peroxide-induced apoptosis in primary cultured mouse hepatocytes. *J. Vet. Sci.* **16**, 17–23 (2015).
35. A. H. Guse, H. C. Lee, NAADP: A universal Ca^{2+} trigger. *Sci. Signal.* **1**, re10 (2008).
36. M. Yamasaki, J. M. Thomas, G. C. Churchill, C. Garnham, A. M. Lewis, J.-M. Cancela, S. Patel, A. Galione, Role of NAADP and cADPR in the induction and maintenance of agonist-evoked Ca^{2+} spiking in mouse pancreatic acinar cells. *Curr. Biol.* **15**, 874–878 (2005).
37. J. B. Parys, H. De Smedt, Inositol 1,4,5-trisphosphate and its receptors. *Adv. Exp. Med. Biol.* **740**, 255–279 (2012).
38. J. Kwon, K. E. Shatynski, H. Chen, S. Morand, X. de Deken, F. Miot, T. L. Leto, M. S. Williams, The nonphagocytic NADPH oxidase Duox1 mediates a positive feedback loop during T cell receptor signaling. *Sci. Signal.* **3**, ra59 (2010).
39. G. Gavazzi, C. Deffert, C. Trocme, M. Schäppi, F. R. Herrmann, K.-H. Krause, NOX1 deficiency protects from aortic dissection in response to angiotensin II. *Hypertension* **50**, 189–196 (2007).
40. D. A. Cockayne, T. Muchamuel, J. C. Grimaldi, H. Muller-Steffner, T. D. Randall, F. E. Lund, R. Murray, F. Schuber, M. C. Howard, Mice deficient for the ecto-nicotinamide adenine dinucleotide glycohydrolase CD38 exhibit altered humoral immune responses. *Blood* **92**, 1324–1333 (1998).
41. A. Flügel, M. Willem, T. Berkowicz, H. Wekerle, Gene transfer into $CD4^+$ T lymphocytes: Green fluorescent protein-engineered, encephalitogenic T cells illuminate brain autoimmune responses. *Nat. Med.* **5**, 843–847 (1999).
42. B.-P. Diercks, R. Werner, D. Schetelig, I. M. A. Wolf, A. H. Guse, High-resolution calcium imaging method for local calcium signaling, in *Calcium-Binding Proteins of the EF-Hand Superfamily: From Basics to Medical Applications*, C. W. Heizmann, Ed. (Springer, 2019), pp. 27–39.
43. A. Worthmann, C. John, M. C. Rühlemann, M. Baguhl, F.-A. Heinsen, N. Schaltenberg, M. Heine, C. Schlein, I. Evangelakos, C. Mineo, M. Fischer, M. Dandri, C. Kremoser, L. Scheja, A. Franke, P. W. Shaul, J. Heeren, Cold-induced conversion of cholesterol to bile acids in mice shapes the gut microbiome and promotes adaptive thermogenesis. *Nat. Med.* **23**, 839–849 (2017).
44. A.-C. Flach, T. Litke, J. Strauss, M. Haberl, C. C. Gómez, M. Reindl, A. Saiz, H.-J. Fehling, J. Wienands, F. Odoardi, F. Lühder, A. Flügel, Autoantibody-boosted T-cell reactivation in the target organ triggers manifestation of autoimmune CNS disease. *Proc. Natl. Acad. Sci. U.S.A.* **113**, 3323–3328 (2016).
45. C. Schläger, H. Körner, M. Krueger, S. Vidoli, M. Haberl, D. Mielke, E. Brylla, T. Issekutz, C. Cabañas, P. J. Nelson, T. Ziemssen, V. Rohde, I. Bechmann, D. Lodygin, F. Odoardi, A. Flügel, Effector T-cell trafficking between the leptomeninges and the cerebrospinal fluid. *Nature* **530**, 349–353 (2016).
46. F. Augsburger, D. Rasti, Y. Cambet, V. Jaquet, NOX5 cell-free assay for the high-throughput screening of small molecules. *Methods Mol. Biol.* **1982**, 103–111 (2019).
47. R. Fliegert, A. Bauche, A.-M. Wolf Pérez, J. M. Watt, M. D. Rozewitz, R. Winzer, M. Janus, F. Gu, A. Rosche, A. Harneit, M. Flato, C. Moreau, T. Kirchberger, V. Wolters, B. V. L. Potter, A. H. Guse, 2′-Deoxyadenosine 5′-diphosphoribose is an endogenous TRPM2 superagonist. *Nat. Chem. Biol.* **13**, 1036–1044 (2017).

Acknowledgments: We thank W. Nauseef, University of Iowa, for providing the DUOX-expressing cell lines to V.J. and K.-H.K. **Funding:** This work was supported by the Deutsche Forschungsgemeinschaft (DFG) (project number 335447717; SFB1328, project A01 to A.H.G. and A.F., project A02 to B.-P.D. and R.W., project A03 to H.-W.M., project A04 to C.M., and project A10 to J.H.) and SCHR1241/1-1, SFB815/TP1, and SFB834 TP2 to K.S., by the Joachim-Herz-Stiftung (Hamburg), Infectophysics Consortium (project 4 to A.H.G.), by NCL-Stiftung Hamburg (to A.H.G.), by the Hamburg Ministry of Science, Research and Equality (LFF-FV75/0070-134, to A.H.G.), and by the University Medical Center Hamburg-Eppendorf (M3I consortium, to A.H.G.). Research in the Guse laboratory is also supported by EU project INTEGRATA-DLV-813284. K.-H.K. is supported by a grant from the Swiss National Science Foundation (project number 31003A_179478). H.G. and J.Y.K. are funded by the NIH (NIH RO1 DK117565-01). **Author contributions:** A.H.G., A.F., K.-H.K., and B.-P.D. conceptualized the project. F.G., A.K., H.G.R., B.-P.D., R.A., D.L., V.J., F.M., L.C.H.C., A.B., A.R., H.G., J.Y.K., K.S., and J.H. curated the data. F.G., A.K., H.G.R., B.-P.D., D.L., A.B., A.R., and J.H. performed the formal analysis. A.H.G., A.F., and B.-P.D. acquired the funding. F.G., A.K., H.G.R., B.-P.D., D.L., V.J., F.M., L.C.H.C., A.B., A.R., H.G., J.Y.K., K.S., J.H., H.-W.M., and K.J.W. contributed to various aspects of the investigations. H.G.R., B.-P.D., D.L., V.J., A.B., H.G., J.Y.K., K.S., and J.H. devised the methodology. A.H.G., A.F., and B.-P.D. supported the project's administration. H.G., K.S., K.-H.K., M.C., A.G.B., and H.-W.M. provided resources, and D.S. and R.W. provided software. F.G., A.K., R.A., B.-P.D., and R.W. contributed to the visualization of the study. A.H.G., A.F., K.-H.K., B.-P.D., H.G., J.Y.K., K.S., K.-H.K., D.L., and A.G.B. contributed to the validations. A.H.G., A.F., K.-H.K., B.-P.D., H.G., J.Y.K., K.S., A.G.B., and K.-H.K. provided supervision. A.H.G. wrote the original manuscript, and all authors reviewed and edited the manuscript. **Competing interests:** The authors declare that they have no competing interests. **Data and materials availability:** A material transfer agreement between the University Medical Center Hamburg-Eppendorf, Hamburg, Germany, and potentially interested academic recipients exists for material produced by The Calcium Signaling Group, Department of Biochemistry and Molecular Cell Biology, University Medical Center Hamburg-Eppendorf. Source data and image analysis software are available from the corresponding author upon request. All data needed to evaluate the conclusions in the paper are present in the paper or the Supplementary Materials.

Submitted 18 August 2020
Accepted 1 October 2021
Published 16 November 2021
10.1126/scisignal.abe3800